Eur. Phys. J. C 40, 447–468 (2005)
Digital Object Identifier (DOI) 10.1140/epjc/s2005-02139-7

THE EUROPEAN
PHYSICAL JOURNAL C

Final results from phase II of the Mainz neutrino mass search in tritium β decay*

Ch. Kraus[1,a], B. Bornschein[1,b], L. Bornschein[1,c], J. Bonn[1], B. Flatt[1], A. Kovalik[1,d], B. Ostrick[1,e], E.W. Otten[1,f], J.P. Schall[1], Th. Thümmler[1,e], Ch. Weinheimer[1,2,g]

[1] Institut für Physik der Johannes Gutenberg-Universität Mainz, 55099 Mainz, Germany
[2] Helmholtz-Institut für Strahlen und Kernphysik, Universität Bonn, 53115 Bonn, Germany

Received: 21 December 2004 /
Published online: 9 March 2005 – © Springer-Verlag / Società Italiana di Fisica 2005

Abstract. This paper reports on the improved Mainz experiment on tritium β spectroscopy which yields a 10 times higher signal to background ratio than before. The main experimental effects and systematic uncertainties have been investigated in side experiments, and possible error sources have been eliminated. Extensive data taking took place in the years 1997 to 2001. A residual analysis of the data sets yields for the square of the electron antineutrino mass the final result of $m^2(\nu_e) = (-0.6 \pm 2.2_{\text{stat}} \pm 2.1_{\text{syst}})$ eV^2/c^4. We derive an upper limit of $m(\nu_e) \leq 2.3\,\text{eV}/c^2$ at 95% confidence level for the mass itself.

PACS. 1460.Pq, 23.40.-s, 2930.Dn, 2930.Aj

1 Introduction

In recent years observations of atmospheric, solar and reactor neutrinos [1–9] in large underground detectors have discovered and established strong mixing among the three neutrino generations ν_1, ν_2, ν_3 produced in weak decays. The mixing manifests itself in neutrino flavor oscillations whose wave numbers are proportional to the differences of the squared masses $\Delta m^2_{ij} =\mid m^2(\nu_i) - m^2(\nu_j) \mid$ of the mixing generations. Neutrino flavor eigenstates ν_e, ν_μ, ν_τ produced in weak interactions with electrons, muons or taus are thus connected to the mass eigenstates ν_1, ν_2, ν_3 through a unitary mixing matrix U. So far oscillations $\nu_e \to \nu_\mu$ and $\nu_\mu \to \nu_\tau$ have been observed yielding mass differences $5.5 \cdot 10^{-5}\,\text{eV}^2/c^4 \leq \Delta m^2_{12} \leq 1.9 \cdot 10^{-4}\,\text{eV}^2/c^4$ and $1.4 \cdot 10^{-3}\,\text{eV}^2/c^4 \leq \Delta m^2_{23} \leq 6.0 \cdot 10^{-3}\,\text{eV}^2/c^4$, taken from a recent combined analysis of oscillation parameters [10].

The fundamental discovery of finite mass differences between neutrino generations has re-stimulated the question about their absolute scale which is left open by any kind of interference experiment, necessarily. It could range from a hierarchical ordering with m^2_1 or m^2_3 being much smaller than either of the measured Δm^2_{ij} values to a quasi degenerate situation where these differences are sitting on a much higher socket $m^2 \gg \Delta m^2_{ij}$ (see e.g. [10]). Assuming $m_1 \approx 0\,\text{eV}/c^2$, the former case would yield $m_2 \approx \sqrt{\Delta m^2_{12}} \approx 0.01\,\text{eV}/c^2$ and $m_3 \approx \sqrt{\Delta m^2_{23}} \approx 0.05\,\text{eV}/c^2$. An experimental hint towards a degenerate solution came recently from a reanalysis [11,12] of earlier, and from new data of the Heidelberg Moscow experiment on neutrinoless double β decay of ^{76}Ge. If due to virtual emission and reabsorption of Majorana neutrinos the observed rate would correspond to a so-called effective neutrino mass

$$m_{ee} = \left| \sum m(\nu_j)\, |U_{ej}|^2\, \mathrm{e}^{\mathrm{i}\phi_j} \right| \tag{1}$$

in the limits $0.1\,\text{eV}/c^2 \leq m_{ee} \leq 0.9\,\text{eV}/c^2$ (99.7% C.L.) [12]. The ϕ are phase factors of the mixing matrix U. Although based on a 4σ signal, this decay mode could still be modified by the exchange of some other non-standard particles.

Since in the universe a huge amount of about 336 relic neutrinos/cm^3 are supposed to be left over from the Big Bang, a sufficient rest mass could play an important role in the total mass balance, in particular as so-called hot dark matter during the early phase of cosmic evolution. Here the fine granulation of fluctuations, observed in the temperature of the cosmic microwave background (CMB) as well as in the large scale structure of the distribution of galaxies (LSS), constrains the neutrino mass. Combined analyses of

---

* This paper comprises principal parts of the PhD theses of Christine Kraus, Beate Bornschein and Lutz Bornschein.

[a] Present address: Department of physics, Queen's university, K7L3N6 Kingston, Canada

[b] Present address: Forschungszentrum Karlsruhe, Tritiumlabor, 76344 Eggenstein-Leopoldshafen, Germany

[c] Present address: Universität Karlsruhe (TH), Institut für exp. Kernphysik, Postfach 6980, 76128 Karlsruhe, Germany

[d] On leave from the Nuclear Physics Institute of the Acad. Sci. Czech Republic, 25068 Rez near Prague

[e] Present address: Helmholtz-Institut für Strahlen und Kernphysik, Universität Bonn, 53115 Bonn, Germany

[f] *Corresponding author*: Ernst.Otten@uni-mainz.de

[g] Present address: Institut für Kernphysik, Universität Münster, 48149 Münster, Germany

recent surveys yield upper mass limits of $0.23\,\mathrm{eV}/c^2$ [13] or somewhat more conservatively $0.33\,\mathrm{eV}/c^2$ [14, 15] assuming 3 degenerate neutrino generations. Another analysis quotes a finite mass of $\sim 0.2\,\mathrm{eV}/c^2$ even [16]. Still there is a caveat in this kind of analysis: it results from fitting a parametrized cosmological model in which 95% of the gravitational potential have to be attributed to unknown sources of matter and energy.

From the above discussion we conclude that a model independent, absolute mass measurement is indispensable even if the sensitivity limit of alternative, model dependent methods is not reached yet.

Among the model independent measurements, the investigation of the β spectrum of tritium near its endpoint has yielded by far the most sensitive limits on the neutrino mass (strictly speaking the mass of the electron antineutrino) in the past. Until the early nineties magnetic β spectrometers prevailed (reviewed in [17, 18]); thereafter electrostatic filters with magnetic adiabatic collimation (MAC-E-Filters) took over thanks to their higher transmission and resolution (reviewed recently in [19, 20]). They were proposed and realized independently in Mainz [21] and Troitsk [22, 23]. Our spectrometer yielded first results in 1991 from which we have extracted an upper limit of $m(\nu_e) < 7.2\,\mathrm{eV}/c^2$ (95% C.L.) [25]; it improved to $5.6\,\mathrm{eV}/c^2$ at the end of phase I of this experiment [26]. These early results still suffered from small spectral distortions far off the endpoint with a tendency to draw the observable $m^2(\nu_e)$ into the unphysical negative sector the more, the farther the spectral interval, used in the analysis, was extended below the endpoint.

After the reason for this effect had been identified, we performed in the years 1995–97 a substantial improvement program. It solved not only that problem but also improved the signal to background ratio by a factor of 10. In 1997 we started phase II of running, yielding in the first year a limit down to $2.8\,\mathrm{eV}/c^2$ (95% C.L.) [27] which was published in parallel to a $2.5\,\mathrm{eV}/c^2$ limit (95% C.L.) from Troitsk [28]. In the second year of data taking our value improved to $2.2\,\mathrm{eV}/c^2$ (95% C.L.), communicated in [29]. This limit was obtained from the experimental result $m^2(\nu_e) = (-1.6 \pm 2.5_{\mathrm{stat}} \pm 2.1_{\mathrm{sys}})\,\mathrm{eV}^2/c^4$. In the present paper we are giving a final report on this experiment, its analysis and its results.

This paper is organized as follows: In Sect. 2 we resume briefly the principle of the experiment and discuss its sensitivity. In Sect. 3 we describe the improvement program carried out for phase II. In Sect. 4 we report on the data taking periods in the years 1997–2001. The data are analyzed and discussed in Sect. 5. In Sect. 6 follows a discussion of the results. Conclusions and outlook are given in Sect. 7.

2 β spectrum and neutrino mass measured by an integrating electrostatic filter

2.1 β spectrum in T_2 decay

Since we observe only the kinetic energy E of the β particle we are measuring actually a sum of β spectra, leading each with probability P_i to a final state of excitation energy V_i of the daughter and with probability $|U_{ej}|^2$ to a neutrino mass eigenstate $m(\nu_j)$. Hence the differential decay rate (Fig. 1) is

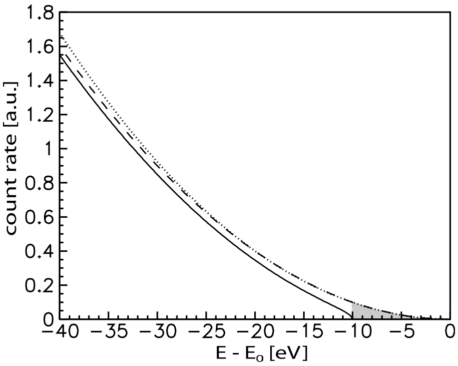

Fig. 1. Tritium β spectrum close to the endpoint E_0. The dotted and the dashed line correspond to $m(\nu_e) = 0$, the solid one to $m(\nu_e) = 10\,\mathrm{eV}/c^2$. In case of the dashed and the solid line only the decay into the electronic ground state of the daughter is considered. For $m(\nu_e) = 10\,\mathrm{eV}/c^2$ the missing decay rate in the last 10 eV below E_0 (shaded region) is a fraction of $2{\cdot}10^{-10}$ of the total decay rate, scaling as $m^3(\nu_e)$

$$\begin{aligned}\frac{\mathrm{d}R}{\mathrm{d}E} &= N\frac{G_{\mathrm{F}}^2}{2\pi^3\hbar^7c^5}\cos^2(\Theta_{\mathrm{C}})|M|^2F(E,Z+1)\\ &\quad\cdot p(E+m_ec^2)\sum_{ij}P_i(E_0-V_i-E)\\ &\quad\cdot|U_{ej}|^2\sqrt{(E_0-V_i-E)^2-m^2(\nu_j)c^4}. \qquad (2)\end{aligned}$$

Here N is the number of mother nuclei, G_{F} the universal Fermi coupling constant, Θ_{C} the Cabibbo angle, M the nuclear decay matrix element, $F(E, Z+1)$ the Fermi function, p the electron momentum, m_e the electron mass and E_0 the Q value of the T_2 decay minus the recoil energy of the daughter. E_0 marks the endpoint of the β spectrum in case of zero neutrino mass. For the decay of molecular T_2 to the ground state of the daughter molecular ion $(^3\mathrm{HeT})^+$ one derives from the most precise direct determination of the mass difference $m(\mathrm{T}) - m(^3\mathrm{He}) = (18590.1 \pm 1.7)\,\mathrm{eV}/c^2$ [30] an endpoint energy of $E_0 = (18574.3 \pm 1.7)\,\mathrm{eV}$ [24] by taking into account the effects through recoil energy and apparative effects[1]. This is in good agreement with [25].

With respect to the required energy resolution, this rather low endpoint favors the choice of tritium. Moreover, the minimal number of electrons in the daughter molecule facilitates the precise calculation of its excitation spectrum (P_i, V_i) in β decay. Another advantage of tritium decay is its superallowed character with a matrix element as large

---

[1] The apparative effects are a combination of electric potential depression, work functions from substrate and electrode system and polarization shift. In the given references [24, 25] the notation E_0 represents the difference in the electrostatic potential of the point the electron starts on the source and the point it crosses the analyzing plane, which we will later describe as eU_0 (see Table 1).

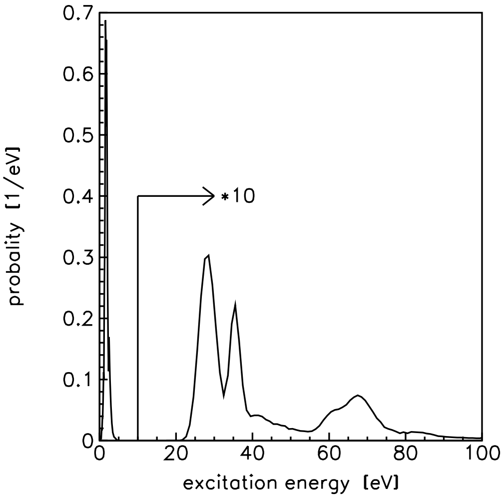

Fig. 2. Excitation spectrum of the daugther $(^3\mathrm{HeT})^+$ in β decay of molecular tritium [38]

as $M = 5.55$ [17]. This leads to a reasonably short half life of 12.3 a and high specific activity of about 3 MBq per cm^2 and monolayer from a frozen T_2 source, in use here.

The Fermi function can be approximated by [31]

$$F = \frac{x}{1 - \exp(-x)} \cdot (1.002037 - 0.001427 \cdot v_\beta/\mathrm{c}), \quad (3)$$

with $x = 2\pi(Z+1)\alpha c/v_\beta$, α is the fine structure constant, v_β the velocity of the β particle. Radiative corrections to the β spectrum have been applied [32,33]. However, they are rather small within our present accuracy limits; they give rise to a shift of $m^2(\nu_e)$ of a few percent of our total systematic uncertainty. One may also raise the point whether contributions from right handed currents might lead to measurable spectral anomalies [34]. We have checked that the present limits on the corresponding right handed boson mass [35] rule out a sizable contribution within our present experimental accuracy [36]. The excitation spectrum (P_i, V_i) of the daughter $(^3\mathrm{HeT})^+$ has first been calculated by Kolos, followed by a number of refined numerical calculations, e.g. [37]. We are using here the most recent ones by Saenz et al. [38]. The excitation spectrum is shown in Fig. 2. The first group concerns rotational and vibrational excitation of $(^3\mathrm{HeT})^+$ in its electronic ground state; it comprises a fraction of P_g=57.4% of the total rate. Its mean excitation energy is 1.73 eV for a β energy close to the endpoint. The same amount of recoil energy goes into the center of mass motion of the molecule and is considered already in the E_0 value given above. In solid T_2 the recoil may excite some phonons in addition. But in the sudden approximation, which is quite valid here, the mean overall recoil energy will even then – for a β energy close to the endpoint – remain at 3.76 eV, which is the ballistic energy the decaying nucleus would receive in classical mechanics.

After this first so-called elastic group we observe an important gap in the spectrum up to the first excited electronic state of $(^3\mathrm{HeT})^+$ at 24 eV. This gap could in principle be filled by a $^3\mathrm{He} + \mathrm{T}^+$ continuum which starts at the dissociation energy of 4 eV. But dissociation at the cost of the β energy is strongly disfavored in the Born–Oppenheimer approximation. At 30 eV the first electronic continuum opens up in which we observe still strong resonances until complete ionization is achieved in the second continuum beyond 80 eV.

In solid T_2 the sudden appearance of an additional nuclear charge may also excite a neighbouring molecule. Kolos et al. [39] have calculated the chance of this spectator excitation to be approximately 5.9% which is taken into account with some modification (see also Sect. 5.6).

2.2 Sensitivity of the β spectrum to $m^2(\nu_e)$

The last two terms in (2) are the total energy E_ν and the momentum p_ν of the neutrino. They represent the neutrino phase space and give rise to the parabolic increase of the β spectrum below E_0 for vanishing neutrino mass, shown in Fig. 1 by the dotted and dashed line. The solid line shows the effect of degenerate neutrino masses $m(\nu_j) = m(\nu_e) = 10\,\mathrm{eV}/c^2$. In case of the dashed and the solid line only the decay into the electronic ground state of the daughter is considered. For $m(\nu_e) = 10\,\mathrm{eV}/c^2$ the missing decay rate in the last 10 eV below E_0 is a fraction of $2 \cdot 10^{-10}$ of the total decay rate, scaling as $m^3(\nu_e)$.

We learn from these numbers that the tiny useful high energy end of the spectrum is threatened by an enormous majority at lower energies. However, it can be rejected safely by an electrostatic filter which can be passed only by electrons with a kinetic energy E larger than a potential barrier qU to be climbed. Any momentum analyzing, e.g. magnetic spectrometer cannot guarantee this strict rejection since scattering events may introduce tails to both sides of the resolution function.

Actually, the $m(\nu_e)$ relevant signature of the spectrum extends further below the shaded triangle of missing count rate in (Fig. 1) into the region where $m(\nu_e)$ causes an asymptotically constant offset. Let us investigate this for a sharp filter which integrates the spectrum for energies $E > |qU|$. For short intervals we may treat all factors in front of the sum in (2) as constant. In this interval it is sufficient to consider only the dominant decay mode into the electronic ground state (Fig. 1). We then obtain the integral count rate

$$\begin{aligned} R(E) &= \sum_j \int_E^{E_0 - m(\nu_j)c^2} \frac{\mathrm{d}R}{\mathrm{d}E'} \mathrm{d}E' \\ &= C_R \sum_j |U_{ej}|^2 ((E_0 - E)^2 - m^2(\nu_j)c^4)^{\frac{3}{2}} + b \\ &= S + b, \end{aligned} \quad (4)$$

where b is the background rate, supposed to be independent of the filter setting and C_R is a specific signal rate. Under practical conditions the signal rate S integrated over the measurement time t separates from the background noise $\sqrt{bt}$ only at distances $E_0 - E$ considerably larger than the sensitivity limit on the mass. There we may develop (4) to first order

$$R(E) = C_R \left((E_0 - E)^3 - \frac{3}{2}(E_0 - E)\sum_j |U_{ej}|^2 m^2(\nu_j)c^4 \right) + b. \tag{5}$$

Besides the leading cubic term this approximate integral spectrum displays a product of the interval length $(E_0 - E)$ and a weighted squared mass

$$m^2(\nu_e) = \sum_j |U_{ej}|^2 m^2(\nu_j), \tag{6}$$

which is our observable. Hence we call the square root of (6) the electron antineutrino mass $m(\nu_e)$ (see also [20]).

The statistical noise $\sqrt{N}$ on the number of counts $N = (S+b)t$ after a measuring time t will be dominated near E_0 by the background and further below by the cubic term. The noise of the latter rises like $(E_0 - E)^{\frac{3}{2}}$ and hence faster than the mass dependent signal. In between there must be a point with optimal sensitivity on $m^2(\nu_e)$; it is found at

$$S = 2b. \tag{7}$$

From a measurement at that point for a time t one would calculate [40] a statistical uncertainty by the help of (5)

$$\delta m^2(\nu_e)c^4 = \left(\frac{16}{27}\right)^{1/6} C_R^{\frac{2}{3}}\, b^{\frac{1}{6}}\, t^{-\frac{1}{2}}. \tag{8}$$

We see that the dependence on the background rate is fortunately much weaker than that on the specific signal rate. For the characteristic parameters of our experiment $C_R = 1.1 \cdot 10^{-5}/\mathrm{eV}^3\mathrm{s}$, $b = 0.015/\mathrm{s}$, one finds the optimal point at 14 eV below E_0 and for the value of (8):

$$\delta m^2(\nu_e)c^4 = 920(t/s)^{-\frac{1}{2}}\,\mathrm{eV}^2. \tag{9}$$

Within 10 days measuring time, (9) drops to $1\,\mathrm{eV}^2$. In an actual experiment one needs of course quite a number of measuring points within a reasonable interval in order to fix also the other parameters C_R, E_0, b and to check the spectral shape in general by a χ^2 fit.

At a particular measuring point E, an endpoint uncertainty δE_0 correlates to $\delta m(\nu_e)^2$ according to (5) as

$$\delta m^2(\nu_e) = \frac{(\partial R/\partial E_0)}{(\partial R/\partial m^2(\nu_e))}\delta E_0 = 2(E_0 - E)\delta E_0/c^4\,. \tag{10}$$

Hence $\delta m^2(\nu_e)$ increases in proportion to the distance from the endpoint, i.e. the neutrino energy E_ν. This is the crux of any missing mass experiment in relativistic kinematics where (10) follows quite generally from the quadratic mass energy relation $m^2c^4 = E^2 - p^2c^2$. That underlines again the necessity of measuring the neutrino mass close to the β endpoint and disfavors any other experimental concept involving energetic neutrinos in order to gain phase space, i.e. the rate.

Instead of fitting E_0 together with the other parameters from the data one could consider to use the known Q value instead [30]. Its error of 1.7 eV, however, would cause through (10) in the most sensitive region, i.e. around 14 eV below the endpoint, an error in $m^2(\nu_e)$ of about $50\,\mathrm{eV}^2/c^4$. This is far beyond our present value obtained from an inclusive fit. The latter is sensitive only to the easily measured small voltage differences in the scan rather than to the absolute energy scale.

On the other hand, we learn from (10) that E_0 should be fitted including somewhat larger distances from E_0, since its uncertainty δE_0 decorrelates from $\delta m^2(\nu_e)$ like $1/(E_0 - E)$. Altogether, there are in principle three spectral regions from which the basic parameters b, $m^2(\nu_e)$, E_0 are fitted most sensitively and with a minimum of cross-talk:
(i) a region beyond E_0 fixing b,
(ii) a region just below E_0 fixing $m^2(\nu_e)$ and
(iii) a region further below E_0 fixing E_0.
In the latter region, however, the inelastic components of the spectrum and their uncertainties start to matter which finally dominate the systematic error. Hence we expect an optimal length of the measuring interval at which we meet a proper balance between the systematic und statistical uncertainty of the result.

3 Improvements of the Mainz MAC-E-Filter

β spectroscopy in the endpoint region by an electrostatic filter is particularly advantageous in combination with an electron optics based on the principle of magnetic adiabatic collimation (MAC-E-Filter) [21,22]. Particles of charge q are transported from the source to the detector by spiraling along the lines of a magnetic field B connecting both (Fig. 3). Hence they can be accepted in the full forward solid angle of 2π, in principle. An electrostatic filter potential U in between is passed if the longitudinal energy $E_\parallel$ along the guiding B-line is larger than qU. In order to filter the full energy sharply the particle momenta have to be well collimated along B. This is achieved by lowering the field strength from a very high value $B_{\max}$ to a quite small one

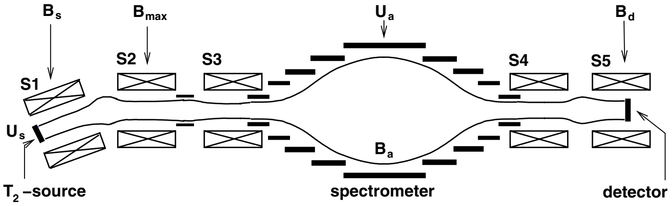

Fig. 3. The improved Mainz MAC-E-Filter is shown schematically. The distance between source and detector is about 6 m and the diameter of the spectrometer vessel is 1 m. From left to right: Frozen T_2 source housed in the tilted solenoid S1; guiding solenoids S2, S3; the vessel with altogether 27 electrodes; refocussing solenoid S4, S5 housing the detector. The shown magnetic field lines confine the flux tube within which the β particles are guided

B_a in the region of the analyzing potential. Thereby the transverse energy in the cyclotron motion $E_\perp$ is reduced adiabatically in proportion to the magnetic field strength and transformed into longitudinal energy $E_\parallel$ along B. In the non-relativistic limit the transformation reads

$$\frac{E_{\perp a}}{E_{\perp \max}} = \frac{B_a}{B_{\max}} = \frac{\Delta U}{U}. \tag{11}$$

Equation (11) defines the relative width $\Delta U/U$ of a MAC-E-Filter. If the field maximum is placed at the source, $B_{\max} = B_s$, then it accepts the full forward solid angle $\Delta\Omega = 2\,\pi$.

In reality we have limited the acceptance to a maximum start angle $\Theta_{\max}$ by placing a field maximum $B_{\max} > B_s$ in between source and analyzing plane acting as magnetic mirror for particles starting at angles $\Theta > \Theta_{\max}$ with

$$\Theta_{\max} = \arcsin\sqrt{B_s/B_{\max}}. \tag{12}$$

Moreover, the angular distribution is slightly modified from isotropy by a scanning potential U_s on the source. Still the transmission function is analytic [41]. For charges $q = -e$ it is given in the four adjacent intervals:

(i) $E - eU_s \leq -eU_a$,

(ii) $-eU_a < E - eU_s < -e \cdot U_a\ B_{\max}/(B_{\max} - B_a)$,

(iii) $-eU_a B_{\max}/(B_{\max} - B_a) \leq E - eU_s \leq E B_{\max}/B_s$,

(iv) $(E - eU_s)/E \geq B_{\max}/B_s$

by

$$T = \begin{cases} 0, & \text{(i)} \\ 1 - \sqrt{1 - \dfrac{E - eU_\mathrm{s} + eU_a}{E}\dfrac{B_\mathrm{s}}{B_a}}, & \text{(ii)} \\ 1 - \sqrt{1 - \dfrac{E - eU_\mathrm{s}}{E}\dfrac{B_\mathrm{s}}{B_a}}, & \text{(iii)} \\ 1. & \text{(iv)} \end{cases} \tag{13}$$

The second line of (13) describes the sharp rise of the transmission from 0 to a plateau within the filter width $\Delta U_s = \Delta U$. The third line describes a further, slow rise of the transmission in the plateau region as a function of an accelerating, thus forward focussing scanning potential U_s on the source until the mirror function of $B_{\max}$ is ruled out in (iv). Transmitted electrons are refocussed by solenoid S4 and hit a silicon detector in the center of another solenoid S5 at a reduced field strength $B_d = 0.31 \cdot B_{\max}$. This limits the angle of incidence to 34°. By the help of auxiliary coils around the central part of the spectrometer, B_a can be varied independently and hence the resolution through (11) and (13). A ratio

$$B_a/B_s > A_s/A_a \tag{14}$$

has to be observed, however, in order to keep the cross section of the beam carrying flux in the analyzing plane well inside the cross section A_a of the cylindrical electrodes. $A_s = 2\,\mathrm{cm}^2$ is the cross section of the T_2 source. We have been running at field ratios down to $B_a/B_s = 3.3 \cdot 10^{-4}$, which limits the flux tube diameter to 88 cm as compared to the diameter of 94 cm of the central electrode.

These relations play a role for the background since the electrodes will emit secondary electrons when they are hit by cosmic rays or any other particles originating from radioactivity. If accelerated toward the detector these electrons will arrive with an energy close to that of the transmitted β particles and cannot be discriminated by the 1.4 keV (FWHM) resolution of the detector. It is important, therefore, that these secondary electrons are being guided adiabatically along magnetic field lines which pass by the detector. Still we observe enhanced background on its outermost ringsegments. Moreover the central guiding field should not be lowered below $B_a \approx 5 \cdot 10^{-4}$ T in order to guarantee full transmission of the 200 eV energy interval under study [40]. Another set of correction coils around the spectrometer annuls the transverse component of the earth's magnetic field and steers the β flux. Runs were performed at settings $B_{\max} = 2.211$ T, $B_a = 5.67 \cdot 10^{-4}$ T, $B_s = 1.087$ T ($\Theta_{\max} = 44.5°$) or $B_s = 1.693$ T ($\Theta_{\max} = 61.6°$), $U_a = -18690$ V, $-20\,\mathrm{V} \geq U_s \geq -320$ V. More details on the general set-up and function of the Mainz MAC-E-Filter have been given in [21,41], and on its recent improvements and performance in [42–44].

3.1 The new source section

In the following we will focus on the various improvements of the apparatus, performed in the years 1995–97 [42]. A decisive improvement concerns the replacement of the LHe bath cryostat by a flow cryostat which allowed one to cool down the T_2-carrying substrate below 2 K by a horizontal cooling section, designed and built by Oxford Instruments on customer's demand. Below that temperature the shock condensed, amorphous T_2 films have been proven to be stable in time. Earlier the source had been operated at temperatures between 3 K and 4 K, at which these films turned out to dewet from the substrate and to contract into small crystals with an average thickness much larger than that of the original film [45–47]. Within these crystals the chance for multiple inelastic scattering events of β particles is enhanced, shifting their energy loss spectrum towards higher losses. Undiscovered, this shift is faking a lower endpoint in the fit which in turn drives $m^2(\nu_e)$ through the correlation (10) into the unphysical negative sector.

This effect is the stronger, the more the data interval extends towards lower energies where it takes in more of these multiple scattered particles. This trend was clearly seen in our first publication, already, and attributed to a yet unidentified additional energy loss component at 75 eV [25]. Actually, this number makes sense to the multiple scattering explanation, since the average energy loss per scattering event is (34.4±3.0) eV [48] and double scattering prevails in these tiny crystals. Duly later, however, we learned about the dewetting possibility of hydrogen films [49] which was not expected to occur below the triple point. We were thus forced to study this phenomenon also for tritium films,

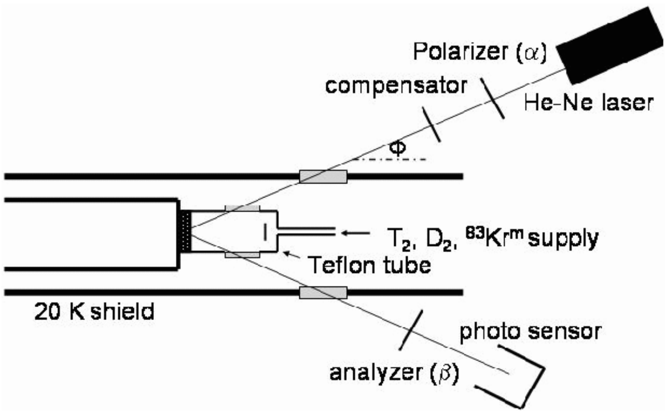

Fig. 4. Scheme of the tritium source with set-up for growing the T_2 film and controlling its thickness by ellipsometry

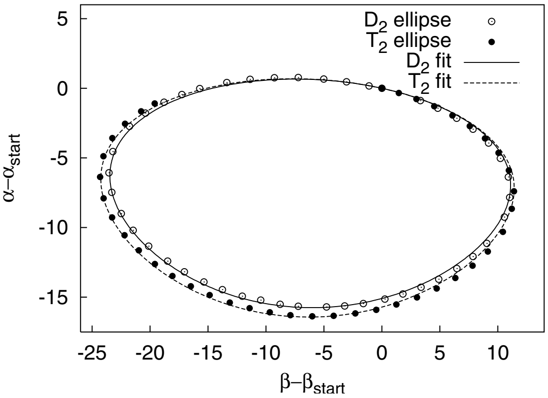

Fig. 5. Control of film growth by ellipsometry for D_2 (open circles) and T_2 (full circles). On the axes are given the corresponding shifts of light extinguishing (α, β) pairs. The lines are fits to the data. The loop closes at the first interference order

determined the decisive activation energy for surface migration to be 45 K and concluded from that on a dewetting time constant $\tau_d \gg 1\,\text{year}$ at $T < 2\,\text{K}$ [47]. The substrate temperature throughout running was $(1.86 \pm 0.01)\,\text{K}$ [2]. Moreover, the source section was upgraded to house a larger ($2\,\text{cm}^2$ instead of $1\,\text{cm}^2$) and thicker source (≈ 140 instead of 30 monolayers of T_2) in order to cope with the strong gaseous T_2 source of the competing experiment at Troitsk [23]. As substrate we have used again highly oriented pyrolytic graphite (HOPG) which combines three advantages:
(i) low backscattering due to the low Z,
(ii) atomic flat surface over wide terraces,
(iii) high purity [50].

The substrate was glued to the copperhead of the cryostat with the silverloaded, heat conducting glue H20E (supplied by Polytec, 76337 Waldbrunn). It withstood cryo as well as baking temperatures of 410 K.

Also the source preparation section has been modified: T_2 gas was released from a heated titanium pellet and fed through a vacuum baked stainless steel capillary and by help of a mechanical UHV manipulator into a cold (20 K) radiation shielding tube which surrounded the substrate (Fig. 4). The precooled gas then entered a teflon cup with an inner cross section of $2\,\text{cm}^2$ which was pressed against the substrate. A kind of diffusor at the inlet ensured a homogeneous molecular flow onto the substrate. The isotopic composition was checked by a quadrupole mass filter. The isotopic T content of the individual sources varied between 63% and 84%. It was considerably improved as compared to phase I.

Radiation shield and evaporation cup were provided with quartz windows passed by a He–Ne laser beam which monitored on line the growth of the source film by ellipsometry. For a given polarization status of the incident beam, the status of the outgoing beam depends through Fresnel's formulas on the reflection from both sides of the film and on the interference of the partial waves. Hence the complex refractive indices $(n_{\mathrm{f(s)}} + \mathrm{i}k_{\mathrm{f(s)}})$ of the film (f) and the substrate (s) enter as well as the film thickness d and the angle of incidence ϕ. Ellipsometry is performed with the help of a polarizer and a $\lambda/4$ compensator in the incident beam and an analyzer in the outgoing beam ahead of a photocell (Fig. 4). Fixing the easy axis of the compensator to $\gamma = 45°$ with respect to the plane of incidence one searches for that pair of polarizer the angle (α) and analyzer angle (β) for which the reflected beam is extinguished. They are functions of the above parameter set [51].

Except for $k_{\mathrm{f}} \approx 0$ the indices are not known a priori with sufficient accuracy. Hence we have grown stepwise rather thick films of D_2 and lately also T_2 up to the first interference order at $d = 4200\,\text{Å}$, determined (α, β) pairs of extinction (Fig. 5) and fitted the parameter set to the data with the results (for the example of Fig. 5) [43]: D_2 film: $n_{\mathrm{f}}(D_2) = 1.148$, $n_s = 2.75$, $k_s = 1.34$; T_2 film $((65 \pm 10)\%\mathrm{T}, (35 \pm 10)\%\mathrm{H})$: $n_{\mathrm{f}}(T_2) = 1.156$. ϕ is measured geometrically to be $(59 \pm 0.3)°$; the fit yields about an equal value and precision for ϕ.

The T_2 films used in the runs are less than 500 Å thick and the measured (α, β) pairs cover only a small section of the full loop, indistinguishable there between D_2 and T_2. The only parameter safely extracted from this short section is the optical film thickness $n_{\mathrm{f}}d$. For our experiment, however, it counts the number column density $\rho_N d$, connected to the refractive index by the Clausius–Masotti relation

$$\rho_N = \frac{n^2 - 1}{n^2 + 2}\,\frac{3}{4\pi\alpha}, \tag{15}$$

with $\alpha = 0.81(1)\,\text{Å}^3$ [52] being the polarizability of hydrogen molecules (for any isotope). From our ellipsometric n_{f} values we thus determine a molar volume of shock condensed D_2: $V_{\mathrm{mol}\,D_2,\mathrm{shock}} = 21.32\,\text{cm}^3$ and of T_2: $V_{\mathrm{mol}\,T_2,\mathrm{shock}} = 20.27\,\text{cm}^3$ [43]. The respective literature values for solid (closely packed) D_2 and T_2 are $19.95\,\text{cm}^3$ [53] and $18.9\,\text{cm}^3$ [54] respectively. The latter is based on calculations. Hence our shock condensed films exhibit a porosity of

$$p = \left(1 - \frac{V_{\mathrm{mol,\,cp}}}{V_{\mathrm{mol,\,shock}}}\right) = 6.4\%\ (D_2) \text{ and } 6.8\%\ (T_2). \tag{16}$$

---

[2] This number corresponds to the reading at the cryostat itself, the absolute precision of the temperature is known to 0.1 K.

This is considered in our later discussion on energy loss.

Up to the year 2000, we have analyzed the ellipsometry of T_2 films using refractive index and molar volume of our shock condensed D_2 films. This leads to a systematic underestimation of the T_2 column density by 1%. Note, however, that the isotopic composition of our T_2 film varies up to 20% leaving still a slight residual uncertainty about the molar volume of the actual film [43]. Moreover, we mention that an alternative calculation of the T_2 column density from the measured count rate leads to qualitative agreement but is not sufficiently precise for a quantitative check.

The optical quality of the graphite surface apparently deteriorated somewhat in time, and led to an increase of the relative error of the film thickness from ±3% (usual case) to +7%/−6% for the worst case of run Q8 (for more details see [42–44]). It is a major contribution to the systematic error through the resulting uncertainty in the energy loss within the source.

After film preparation the source is pushed into the front end of a LHe-cooled chikane, which spans throughout the kinked solenoids S1 und S2. It is the second important improvement of the source section. Evaporating T_2 is adsorbed on its carbon coating and the straight flight into the spectrometer is prevented by its 20° bent, whereas the magnetized charged particles follow the equally bent field lines. The cryotrap totally rejected any source dependent background which earlier made up half of the background rate, even for much thinner sources.

The cryotrap also suppressed condensation of rest gas (predominantly H_2) from the spectrometer onto the T_2 film. Still we have observed by an ellipsometric check at the end of a run a certain growth of the film thickness by 0.14 monolayer/day. The source activity, on the other hand, decayed with an apparent lifetime of about one year. Obviously the recoiling daughter molecules each sputtered a handful of neighbouring molecules off the source.

3.2 Electrode and HV system

The design of our spectrometer has been aiming at a short, economic instrument with high resolution, that is a high field ratio $B_{\max}/B_a$. Consequently it has sharp B gradients which endanger adiabatic motion. Therefore, we have tried to compensate this drawback by decelerating and reaccelerating the particles partly in the high field within the solenoids S3 and S4. This was provided by a series of ring electrodes.

However, field emission by the strong electric field and particle storage by the strong magnetic field together favor the development of plasmas even under UHV conditions. Such plasmas lead to an untolerable background rate at field settings $B_{\max} \geq 2\,\mathrm{T}$. Hence the spectrometer could not be operated up to its limit of $B_{\max} = 8.6\,\mathrm{T}$ where adiabaticity would be observed best [21].

Therefore, the improvement phase also included a redesign of electrodes No. E6 to E11 in the high B field [42]. Their number was increased by 2 (E12, E13) in order to smoothen the potential drops and titanium was chosen instead of copper for reasons of lower field- and X-ray emission. The latter was suspected to produce through secondary reactions a background component observed about 5 keV above the filter potential whose tail still extends into the accepted energy window of the detector [21, 55, 56]. Moreover, these electrodes were reshaped such that they include about the same magnetic flux ($\approx 6\,\mathrm{T\,cm}^2$) everywhere. The new electrode system performed better in so far, as the mentioned background component disappeared, indeed, and a breakdown voltage of −30 keV could be reached safely within a shorter conditioning phase.

But still the plasma induced background rate rose beyond $B_{\max} \approx 2\,\mathrm{T}$. In the presently running phase III of the experiment, which comprises an extensive background exploration and reduction program to prepare the follow-up experiment KATRIN [57], we have removed the multi-electrode system from the high field region and retained only a few central electrodes, all set to the full analyzing potential. Now the spectrometer is stable up to the highest B field, in accordance with earlier experience at the Troitsk spectrometer. For this latter, non-bakable instrument no stable running mode was found at all with the original multi-electrode system [58].

The filter potential U_a was provided by a highly stabilized HV power supply (model HNC5 30000-5 by Knuerr Heinzinger, 83026 Rosenheim) directly connected to the central electrode. The potentials of the other electrodes (requiring less precision) were derived from U_a by a home-made resistive voltage divider. U_a was monitored and read out continuously by two different systems: The first system comprises a high-precision digital voltmeter (model DMM 6048 by PREMA, 55129 Mainz) which was connected to U_a via a precision voltage divider, $1:5000$ (model KV 50 by Julie Research, New York, USA). In the second system the voltage U_a was divided by $1:50$ by a second voltage divider (model KV 50 by Julie Research, New York, USA) and the difference to a voltage standard (model 335A by Fluke) was measured by a precision digital voltmeter (model DMM 5040 by PREMA, 55129 Mainz). The observed short- and long-time fluctuations comply with the specifications of the instruments. To check the HV equipment the K(32) conversion line of ^{83m}Kr was measured before or after each tritium run. The values show a small drift from Q2 to Q12 but the difference to the fit values for U_0 (given in Table 1) of 1998–2001 can be summarized as $749.5 \pm 0.5\,\mathrm{eV}$ and appear reasonable compared to the specification of the HV chain. To control the stability during a measurement periode, we analyzed shorter time intervals and compared the resulting retarding voltages which are found by the fit for the endpoint values. They agree within their statistical uncertainties.

The scanning potential in the range $-320\,\mathrm{V} \leq U_s \leq -20\,\mathrm{V}$ was provided by a fast computer controlled power supply model HNC10 3500-10 by Knuerr Heinzinger, 83026 Rosenheim and applied to the electrically insulated source. A high-precision divider (Fluke) and a high-precision digital voltmeter (model DMM 5017 by Prema, 55129 Mainz). The minimum negative bias of −20 V prevents that recoil ions emitted from the source are accelerated into the spectrometer where they cause a high background rate through rest gas ionization [25].

3.3 Spectrometer vacuum and conditioning

The improvement program also comprised electropolishing of the spectrometer tank and its electrodes, in order to reduce outgassing and field emission but also for removing any tritium contamination from phase I when we were running without the protection by the cryotrap. Also the 80 m of getter strip (type ST 707/CTAM/30D by SAES, Milano, Italy), mounted onto the inner surface of electrode E2 were renewed. It represents a pumping speed of 18 m^3/s for hydrogen. The spectrometer was pumped in addition by two turbomolecular pumps at 500 l/s each.

Once a year the spectrometer was baked for about a week reaching a maximum temperature of 330°C to 420°C for about 24 hours, at which also the getter was activated. Thereafter the rest gas pressure (mainly H_2) reached a level of better than 10^{-10} mbar. Although we could not observe any deterioration of the vacuum in between, the performance of the spectrometer apparently improved after a very intense rebaking in 2001 in the sense that tiny anomalies appearing in the spectra of runs Q9 and Q10 in 2000, did not occur anymore, thereafter.

In addition to electropolishing and baking, conditioning of the spectrometer up to ±30 kV, well above the operating voltage of 18690 V (neg.), proved to be necessary to prevent any sparkings or minisparkings during runs. The latter are not observed in the electric circuit but manifest themselves by an outburst of background events which die out quite slowly such that a whole scan (passing all measurement points twice) has to be rejected. In the runs of 2001 (Q11, Q12), not a single background burst has been observed. In all earlier runs they appeared about once a week.

3.4 β-detection and data acquisition

Transmitted β particles are detected by a silicon detector which is segmented into five circular rings of 1 cm^2 area each. Usually only the three inner segments are considered for data evaluation; the fourth displays already enhanced background which increases towards the spectrometer walls. The radial segmentation is also useful for accounting for the potential drop which occurs in the center of the analyzing plane and achieves $4 \cdot 10^{-5} U_a$ on axis.

For phase II the possibly contaminated old detector was replaced by a new one with a still thinner dead layer but otherwise identical specifications (B1256 by Eurisys Mesures, France). The energy loss in the dead layer was determined to be about 200 eV at $E = 18$ keV, corresponding to a mass layer of about 15 µg/cm^2. The detector together with the attached preamplifiers were cooled down to ≈ -80°C. The preamplified signals were fed out of the vacuum for further amplification and pulse height analysis. Details are given in [59,60].

Backscattered electrons are remirrored onto the detector within its intrinsic time resolution. They contribute to the low energy tail of the signal with an energy loss by multiple passage through the dead layer. Figure 6 shows the detector response to the last 200 eV of the tritium β spectrum. The FWHM is 1.4 keV, the accepted energy window 15 keV to 21 keV. Reinforcement of low level lead shielding and removal of some potassium containing material reduced the background from environmental radiation by a factor of 3 down to a rate of $4.6 \cdot 10^{-5}/(\mathrm{s\,keV})$ on each segment. Moreover, the vacuum conditions of the detector housing were improved to UHV standards in order to allow for removal of the thin foil which earlier had separated it from the much better spectrometer vacuum. It had deteriorated the energy distribution of the passing β's [21]. Instead an open, getter coated tube was installed serving as an active differential pumping section [42].

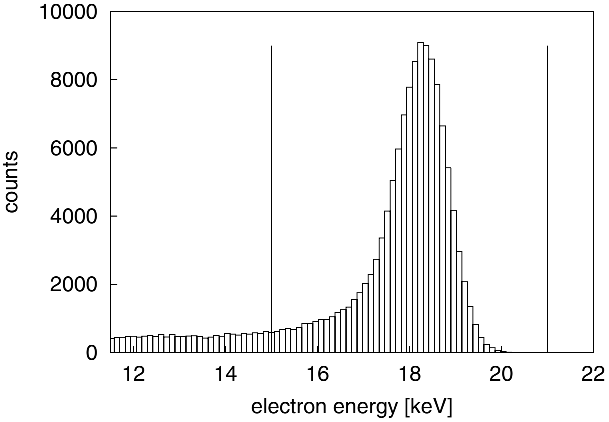

Fig. 6. Detector response to the last 200 eV of tritium β decay. The perpendicular lines indicate the accepted window (15–21 keV)

At fixed energy window of the detector its efficiency slightly increases with β energy due to the asymmetric signal slope. By offsetting the β spectrum at the source the respective coefficient was determined to be $\alpha_d = (4 \pm 2)\%/\mathrm{keV}$. It is considered in the analysis with marginal effect. The low count rate of less than 250 Hz allows one to acquire the data event by event without suffering substantial losses by signal processing and read out, requiring altogether 63 µs [3]. Pile up rejection raises no problem in view of the time constant of 3 µs of the analogue circuit. Since any enhanced pile up rate points to electronic noise or some other pertubation it is recorded in order to reject such periods in the off line analysis. The event protocol comprises height and real time of the event. Moreover, its time difference to the foregoing event is recorded with a resolution of 100 µs for the purpose of correlation studies. Scanning of the spectrum via the source potential U_s is PC controlled. Usually a measuring time of 20 s per data point was chosen. Their distribution has been adjusted to ensure a properly weighted sensitivity to the decisive fitting parameters. Figure 7 shows the example of runs Q11 and Q12. Other runs had a somewhat different distribution and number of measuring points. The potential differences between the data points are ramped with soft slopes over 3 s in order to prevent particle trapping by sharply rising potential walls. A total scan comprises an up and a down scan. At the end of each data point the filter and source po-

---

[3] From 2000 on this number was decreased to 50 µs due to a faster computer for data acquisition.

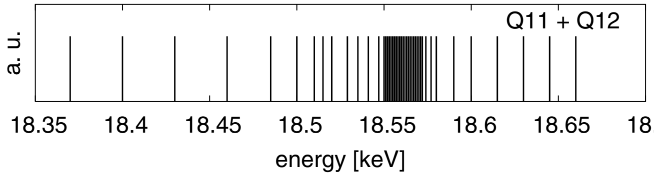

Fig. 7. Distribution of the 45 measurement points in runs Q11 and Q12. In the dense region their spacing is 1 eV

tentials U_a, U_s are read out and stored. Moreover a number of other important control parameters such as the source temperature, the He throughput through the cryostats, the status of the vacuum system etc. are monitored.

Any considerable deviation from normal status activates an automatic control and safety system which communicates the malfunction as short message via mobile phone to the operators in charge. It also performs a safety shutdown if necessary. Vice versa the operators could access the control system at any time and read out the essential parameters remotely. Except for serving hours, therefore, the experiment was running around the clock in a stand alone mode, a necessity in view of the small crew involved.

4 Measurements in phase II, 1997–2001

4.1 Spectrometer background

Figure 8 shows a typical background spectrum from the spectrometer as measured by the detector with the T_2 source closed off, either mechanically by a valve in the beam line or just with respect to the β particles by a filter potential above E_0. The installation of the bent cryotrap has totally suppressed any source dependent background as said before. On top of a smooth continuum one observes a single peak. A high statistics analysis has shown that its mean coincides with the filter potential within an uncertainty of about 30 eV. Most probably this peak is a sharp line, actually, stemming from electrons, produced at low energy somewhere in the large analyzing volume of the spectrometer or at the surface of the respective electrodes, and then accelerated by the filter potential towards the detector or the source. According to (11) this is possible, if their transverse energy $E_{\perp a}$ is less than the filter width of about 4 eV. Otherwise they will be trapped magnetically within the B field minimum in the center.

The rate of this background, which we cannot distinguish from the β particles, ranges from about 12 mHz in the very best cases of the last runs Q11 and Q12 up to the order of 50 mHz at poorer performance. The numbers from the similar Troitsk experiment are quite comparable.

The phenomenology of our spectrometer background has been studied extensively in a number of theses over the years [21, 56, 61–66]. The qualitative insight obtained thereby was very instrumental for improving to the present satisfactory status. But the various mechanisms at work are complex, apparently, such that they could not be identified and disentangled clearly and pinned down quantitatively, neither by experiment nor by simulation. Only the radical hardware measures during the presently running, background dedicated phase III are giving experimental access to a somewhat better understanding of the underlying mechanisms [63–66]. Thus routes for further background suppression are opened for KATRIN. Since this will be subject of a forthcoming paper [67], we will confine the background discussion in this paper to the context of phase II runs and results.

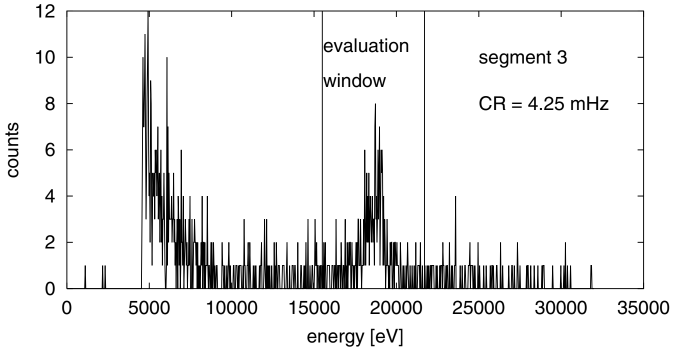

Fig. 8. Spectrometer background spectrum, collected for 13 h on detector segment 3. The perpendicular lines indicate the accepted energy window for evaluation

From background studies with external γ and X-ray sources and from coincidence with passing cosmic muons, it seems to be clear that an important background component – if not all of the observed "hard core" of 12 mHz – consists of secondary electrons emitted from the inner surface of the large central electrodes. In perfect adiabatic motion they would spiral along peripheral flux lines which pass by the detector. However, the actual electromagnetic configuration with its rather weak central B field in combination with radial E field inhomogeneities seems to give them a chance to drift into the sensitive flux tube on a non-adiabatic path. From muon coincidences we learned that at least part of them arrive within a few µs. At UHV conditions, these events cannot be affected anymore by rest gas collisions. Recently we have found that such electrons can be rejected by a grid at some repelling potential [63].

Contrary, a single high energy electron, as e.g. from T_2 decay within the sensitive flux tube of the spectrometer, may well be stored magnetically for minutes and cause background events by rest gas ionization with an average rate of the order of the observed one at a vacuum of 10^{-10} mbar. At 10 times higher pressure this background source can be recognized (and also eliminated at low signal rate) as a relatively fast chain of correlated events [23]. Also minisparks or field emission may end up eventually in such trapped high energy electrons.

Guided by such hypotheses we have applied RF pulses of (1.0–1.8) MHz and up to 180 V amplitude onto particular electrodes in order to heat up such trapped electrons stochastically and expel them [27, 61]. This attempt turned out successful, in fact, when the RF pulse was applied to electrode E8 on the detector side which is at a DC potential of $0.86U_a$. The RF was applied for (1–2) s each time, during the pause when the scanning voltage was changed. In run Q5 for example we thus managed to reduce the

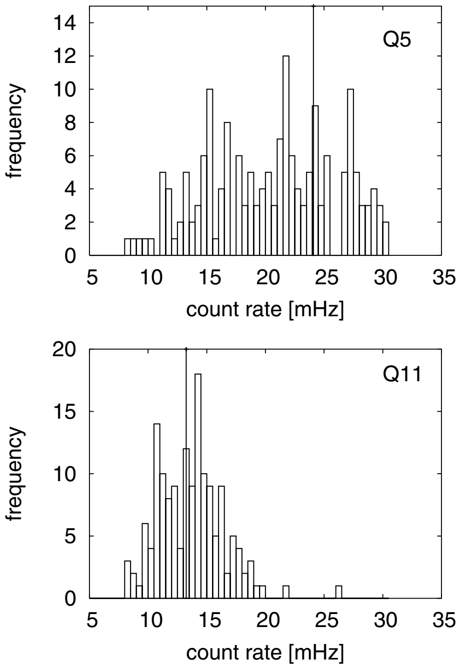

Fig. 9. Histograms of background rates during the measurements Q5 and Q11. Each entry is an average over 8 scans, where the measurement time in the background region adds up to 600 s for each scan

background rate from an unsatisfactory level of 50 mHz down to ≈ 20 mHz [27].

Figure 9 shows two histograms of background fluctuations, the one from run Q5 with pulsing, the other from run Q11 without pulsing. In the former case pulsing did reduce an enhanced background to an acceptable average rate of $\bar{b} = 21.6$ mHz. But the fluctuation is apparently wider than $\sqrt{bt}$, expected from ordinary statistics. This makes sense, since enhanced background rates during the occasional presence of ionizing trapped electrons obey a kind of Levi statistics with irregular fluctuations. On the other hand, the low and steady "hard core" background of $\bar{b} = 12.6$ mHz, achieved in Q11, displays a nearly ordinary fluctuation.

At UHV conditions, also the build-up and decay of trapped plasmas will occur on longer time scales [21]. A certain phase space of electrons can be trapped everywhere within the sensitive flux tube of the spectrometer, either by magnetic mirroring at both necks of the magnetic bottle or only at one of them and electrostatic reflection at the central filter potential.

Outside the sensitive flux the stepwise increase of the diameter of electrodes forms small equipotential corners crossed twice by magnetic field lines. This is the electromagnetic configuration of Penning traps. Electrons released from plasmas in such traps may eventually find their way to the detector. Also ions from such plasmas, positive as well as negative ones, can contribute to the background by secondary reactions as said before.

If trapped plasmas are fed at least partly by β particles from the source, then the background they produce will depend on the β flux therein, which varies with the scanning potential of the source. Such a kind of cross-talk between scanning and background could be the origin of the tiny residual spectral anomalies which have been observed in few of the runs and reported already in [27]. Their amplitude is on the level of mHz, i.e. of order 10% of the total background rate. The slow build-up and decay rates of stored particles may also give rise to the hysteresis of these anomalies which has been observed between up and down scanning in run Q9.

In a pulsed mode of running, the technique of which has been described in [68], we have searched for a background dependence on the scanning voltage in a time window ranging from a few µs to 30 min after shutting off the signal rate by a positive pulse on the source. Within statistical limits of 1 mHz we did not observe any correlation between the background rate in the pauses and the signal rates in the open phases of the spectrometer [62]. This negative result does not really contradict our presumptions on the possible origin of the residual spectral anomalies, since these have only rarely occured at non optimal conditions.

A total stability of the background rate over the full running period has been observed for runs Q11 and Q12.

4.2 Discussion of runs Q1 to Q12

In Table 1 we have listed characteristic parameters of all 12 runs Q1 to Q12 performed with the improved set-up in the period 1997 to 2001. They covered an interval from 18370 V up to 18860 V, i.e. from 200 eV below to 90 eV above E_0 (Fig. 7).

We should mention that we fitted the parameter $m^2(\nu_e)$ as really free parameter without constraints. In order to account for statistical fluctuations of the data the fitting routine[4] requires a mathematical continuation of the spectrum into the region $m^2(\nu_e) < 0$ which provides a symmetric χ^2 parabola around $m^2(\nu_e) = 0$ for a statistical data sample. This purpose is fulfilled quite well by introducing factors f_i to each electronic final state in (2) defined by

$$f_i = \Theta(-m^2(\nu_e))\Theta(\epsilon_i + \mu)\left(1 + \frac{\mu}{\epsilon_i} e^{-(1+\epsilon_i/\mu)}\right) + \Theta(m^2(\nu_e))\Theta(\epsilon_i - m(\nu_e)c^2), \qquad (17)$$

with $\epsilon_i = E_0 - V_i - E$, $\mu = -0.66\, m^2(\nu_e)c^4$ [25]. For negative $m^2(\nu_e)$ they stretch the spectrum smoothly beyond the respective endpoint up to $E_0 - V_i + \mu$. The negative $m^2(\nu_e)$ sector might also be fitted by a physical model, namely the β spectrum arising from tachyonic neutrinos [69]. But this point would come up only in case of an unambiguous experimental negative $m^2(\nu_e)$ result. Summarizing, negative

---

[4] The shape of the β spectrum near the endpoint is mainly defined by the factor $(E_0 - E)\sqrt{(Q-E)^2 - m^2(\nu_e)c^4}$ which can be expanded for $(Q-E) \gg m(\nu_e)c^2$ into $(E_0 - E)^2 - m^2(\nu_e)/2$. Therefore for a neutrino mass around zero any fluctuation of the count rate downwards yields a positive value for $m^2(\nu_e)$ and versus any fluctuation upwards should result in a negative value of the parameter $m^2(\nu_e)$.

Table 1. Parameters for measurements Q1-Q12 of phase II. $\Theta_{\max}$ is the maximal opening angle, t is the running time, pt the number of different measurement points, ft the film thickness, $\bar{b}$ the average background rate, $m^2(\nu_e)$ is the fit result for the last 70 eV, and U_0 is the retarding voltage at which the fit finds an endpoint value

no.	$\Theta_{\max}$	t [d]	pt	ft [nm]	$\bar{b}$ [mHz]	$m^2(\nu_e)$ [eV^2]	U_0 [V]
Q1	45°	6		20.8		test measurement	
Q2	45°	26	50	96.7	16.7 ± 0.3	-11.2 ± 6.0	18573.5 ± 0.3
Q3	45°	24	64	49.3	12.7 ± 0.2	-14.8 ± 4.6	18574.0 ± 0.2
Q4	45°	38	64	49.5	11.7 ± 0.2	-3.9 ± 4.7	18574.5 ± 0.2
Q5	45°	46	64	47.5	21.6 ± 0.2	-3.5 ± 6.0	18574.4 ± 0.2
Q6	62°	38	33	43.0	12.5 ± 0.2	$+0.4 \pm 7.2$	18575.7 ± 0.2
Q7	62°	29	33	43.2	14.3 ± 0.2	-2.4 ± 4.9	18575.4 ± 0.2
Q8	62°	54	39	45.5	16.5 ± 0.2	-0.9 ± 4.8	18576.2 ± 0.3
Q9	62°	56	39	44.4	18.6 ± 0.3	-10.9 ± 3.2	18575.1 ± 0.2
Q10	62°	35	45	45.5	16.6 ± 0.3	-6.1 ± 4.8	18574.6 ± 0.2
Q11	45°	31	45	48.2	12.6 ± 0.2	$+1.3 \pm 5.8$	18576.7 ± 0.2
Q12	62°	19	45	48.5	12.6 ± 0.2	-1.0 ± 6.0	18576.6 ± 0.2

values for the fit parameter $m^2(\nu_e)$ are not necessarily unphysical but should be obtained within statistical limits as a result of an unconstrained fit in 50% of all data sets if the neutrino mass is around zero.

In the following we will report on each of the 12 runs performed in phase II irrespective of wether it has been selected for the final data set. Thus we take the chance to discuss carefully experimental effects on the given example which might lead to spectral anomalies and systematic uncertainties if undiscovered.

Q1 and Q2

The first run Q1 was devoted to a short test experiment with a relatively weak T_2 source. We observed in particular that the background due to T_2 evaporation into the spectrometer and decay therein had disappeared as said above. Encouraged by this success we have produced a very thick source Q2 of 967 Å corresponding to 284 monolayers. At this thickness the rate of β particles which leave the source without energy loss is already close to its maximum possible value obtained from an infinitely thick source. Running this high source activity turned out to be smooth and stable without any source dependent background problems.

However, the analysis of the data revealed an average shift of the endpoint by -3 eV. This effect was then systematically investigated by freezing ^{83m}Kr activity on top of T_2 films and measuring precisely the energy of its 17.8 keV conversion line as a function of the film thickness. In this way we have discovered that the film charges up positively by 21.2 mV per monolayer. The corresponding electric field strength of 62.6 MV/m is necessary to release the positive charges, left over from β decay, from their trapping potential within the T_2 lattice. These first experiences with the improved set-up have been communicated in [70]. A thorough analysis of source charging is given in [71]. The linear increase of the charge up voltage throughout the film has to be folded into the transmission function and results in a broadening in addition to an average shift. A systematic uncertainty in the broadening effect of Gaussian shape with variance σ^2 would yield an uncertainty in $m^2(\nu_e)$ by $-2 \cdot \sigma^2$ [72]. Therefore, we have reduced the film thickness by a factor of 2 in later runs. Moreover the uncertainty of the energy loss weighs heavier in a thick source than in thinner ones. Still, as compared to phase I results, the analysis of Q2 led to a reduction of the unphysical negative $m^2(\nu_e)$ value by an order of magnitude (see Fig. 13 in Sect. 5).

Q3 and Q4

One might have expected that the residual small negative $m^2(\nu_e)$ of order $-10\,\mathrm{eV}^2/c^4$ still observed in run Q2 would disappear with thinner sources. However, the following runs, Q3 and Q4, showed the same problem at similar size but with somewhat different dependence on the fit interval. Moreover, the clearly enhanced χ^2 values obtained in fitting Q2, Q3 and in particular Q4 pointed to some residual spectral anomalies in the data (see Fig. 13). The Troitsk group had already reported on a steplike anomaly which appeared in their integral spectra with an amplitude of order 10^{-10} of the total decay rate and at variable positions in the range from 5 to 15 eV below the endpoint. The change in time of the positions of these steps seemed to be compatible with a half year period, even [28]. If attributed to a general physics phenomenon, e.g. a monochromatic line in the β spectrum of T_2, it should appear in our spectra equally. Fitting such a step into the Q4 spectrum led to a significant reduction of χ^2, and lifted $m^2(\nu_e)$ to an acceptable value of $(-1.8 \pm 5.1_{\mathrm{stat}} \pm 2.0_{\mathrm{sys}})\,\mathrm{eV}/c^2$, indeed [27]. Also the position at 13 eV below E_0 and the amplitude of the step of about 6 mHz accorded to the Troitsk picture. In the following runs it was an important issue, therefore, to investigate further and – if possible – eliminate these residual spectral anomalies.

Q5 to Q8

Ahead of run Q5 we found out that an enhanced and fluctuating background rate could be reduced essentially by applying an RF pulse to electrode E8 on the detector side as has been reported above. In particular Q5 profited from this procedure; it reduced the averaged background rate from 50 mHz down to 21.6 mHz. Q5 was also the first run whose analysis did not reveal any spectral anomaly any more but yielded an $m^2(\nu_e)$ value compatible with zero at good χ^2 for any data interval (see Fig. 13).

Still the background rate was higher in Q5 than in the foregoing runs which suffered from slight residual anomalies. Apparently these anomalies do not correlate necessarily to a higher average background; but a correlation between background events and the operating cycle of the spectrometer – which clearly produces an anomaly – can occur also at low average background. At that point we recall that the anomalous count rate does not exceed a few mHz and hence constitutes at most a small fraction of the background rate. On the other hand the facts seem to corroborate the assumption that the removal of trapped electrons by pulsing also may brake the correlation between background and operating cycle. Run Q5 was the basis of our result $m^2(\nu_e) = (-3.7 \pm 5.3_{\text{stat}} \pm 2.1_{\text{sys}})\,\text{eV}^2/c^4$ with the limit $m(\nu_e) < 2.8\,\text{eV}/c^2$ (95% C.L.) published in 1999 [27]. But also the series of data collected in the runs Q3 to Q5 could be analyzed successfully in a so-called "15 eV analysis". Besides the background region above E_0, only the last 15 eV of the spectrum were considered here together with two more data points further down at 18470 eV and 18500 eV respectively; they were necessary to fix E_0 with sufficient precision. Thus the "troublesome" region of anomalies was excluded mostly from the fit. The result was $m^2(\nu_e) = (-0.1 \pm 3.8_{\text{stat}} \pm 1.8_{\text{sys}})\,\text{eV}^2/c^4$, which leads to an upper limit of $m(\nu_e) < 2.9\,\text{eV}/c^2$ (95% C.L.) [27].

In between runs Q5 and Q6 the spectrometer was baked again to a maximum temperature of 394°C and HV conditioned. The procedure resulted in a background reduction down to 12.5 mHz observed in Q6. This rate was independent of pulsing as proved by the no pulsing mode which ran alternatively every second day. Q7 was running in the same alternating manner. Without pulsing the background had now increased to 14.7 mHz (the number given in Table 1), whereas it remained essentially stable at 12.7 mHz in the pulsing mode. Permanent pulsing was applied to run Q8, the background had increased further to 16.5 mHz. Note that these numbers are averages over the full running period. Without pulsing the background was slowly rising in real time and had to be set back by reconditioning the electrode system a few times during a run.

On the thirty-first day of run Q8 the "apparent" lifetime of the source (as measured from the course of its activity) increased from 300 to 620 days. The event was caused by a sudden coverage of the source with a couple of monolayers of H_2, which had been collected before from the residual rest gas onto the shield in front of the source. From there it was released then during a short cooling failure of the shield and partly recollected onto the still cold source. The data from the remaining period yielded a significant negative $m^2(\nu_e)$ value, caused by the additional energy loss in the H_2 cover. Also under regular conditions the shield could not completely prevent a slow and steady condensation of residual H_2 onto the source. A daily coverage by 0.3 monolayers was estimated from ellipsometry (see above) and considered in the analysis causing a small, still significant effect (see below).

The analysis of the data set Q6 to Q8 yielded stable fit results of $m^2(\nu_e)$ close to zero at any data interval and with a good χ^2 (see Fig. 13). Together with Q5 it improved the result to

$$m^2(\nu_e) = (-1.6 \pm 2.5_{\text{stat}} \pm 2.1_{\text{sys}})\,\text{eV}^2/c^4, \qquad (18)$$

from which an upper limit of $m(\nu_e) < 2.2\,\text{eV}/c^2$ (95% C.L.) was extracted. This result has been communicated at the Neutrino 2000 conference [29] and cited thereafter frequently.

Q9 to Q10

The long period of data collection in runs Q5 to Q8 was followed by a number of systematic background studies [61, 62], the results of which have been summarized above already. Thereafter tritium measurements were immediately resumed in Fall 2000 without a break for extended maintenance. Since the last baking of the spectrometer, which apparently had not reached the temperature of the earlier ones, six months had elapsed. Although running was quite smooth at a moderate background rate of 20 mHz, the on line analysis of the Q9 data showed rather soon a reappearance of slightly negative $m^2(\nu_e)$ values around $-10\,\text{eV}^2/c^4$. Nevertheless we continued measuring since parallel runs were foreseen at Troitsk in order to check whether any Troitsk anomaly would appear synchronously in both experiments. We also refrained from any interference by reconditioning the electrodes like in earlier runs. Rather we decided to watch how the running conditions and results would develop in time in the two alternating modes of cleaning and not cleaning the spectrometer from stored particles by RF pulses.

An apparent anomaly of Q9 is a hysteresis of count rate between up and down scanning: It is visible in the raw spectra already (Fig. 10). Analysis shows that the effect was much stronger in the non-pulsed than in the pulsed mode. The effect also diminished when the final approach to each measuring point was performed always from the same side, namely from a higher voltage level; that means, upramping was performed by first overshooting the proper value and then pulling back as if it were downramping. The hysteresis clearly indicates the presence and influence of stored particles, whose accumulation and/or loss conditions correlate by some mechanism to the setting of the spectrometer. The instability of background conditions introduced this way is also witnessed by an enhanced scatter

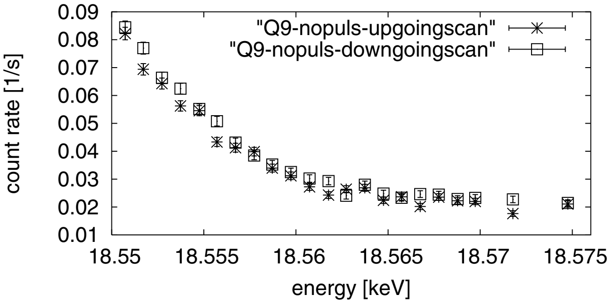

Fig. 10. Hysteresis effect in run Q9 during periods without background suppression by pulsing. Squares correspond to scanning towards the endpoint, crosses to the opposite direction

in Q9 as discussed above and shown in Fig. 9 for the example of Q5. Even if the exact mechanism has not been cleared up yet in detail, the knowledge of its phenomenology is already very important for the experimentalist and enables to prepare cautious countermeasures.

In the following run, Q10, the measuring points have not been addressed in a monotonous voltage sequence but in a random generated one. Unfortunately, the software did not allow for a fresh random choice each scan without major changes. But the same sequence was repeated forth and back for the whole run. Still this was sufficient to suppress the conspicuous hysteresis of Q9, not so the occurrence of trapped particles as such, however. Hence also the Q10 spectrum is slightly impaired by the imperfect running conditions, leading to a negative $m^2(\nu_e)$ result in summary (see Table 1). The Q9 and Q10 data have also been analyzed in weekly time bins. They show fluctuations of the $m^2(\nu_e)$ fit result which exceed the statistical limits. Hence Q9 and Q10 data were not considered in the final fit.

In spite of being slightly impaired, the Q9 and Q10 spectra did not display any indication of a steplike Troitsk anomaly, neither in the full data sets, nor in binned ones. This holds in particular for the time bins 6.12.–13.12. and 22.12.–28.12.2000 where the Troitsk experiment was running in parallel to ours. In both periods Troitsk, however, observed the sudden outburst of significant steps. In the second period it even reached an amplitude of 14 mHz (discussed further below).

Q11 and Q12

The experience of Q9 and Q10 has taught us again the importance of optimal maintenance ahead of running, although the vacuum had been fine all the time. Changes in surface conditions seem to rule field emission of electrons and/or ions which fill residual traps and interfere with the measurement. Hence the spectrometer was rebaked at a maximum temperature of 373°C for 13 h. Thereafter, the electrodes were conditioned up to ±30 keV with reinforced sparking at a residual hydrogen pressure of 10^{-7} mbar, obtained by heating up the SAES getters at closed turbo pumps. Also the source section was thoroughly maintained including exchange of source substrate and T_2-pellet, baking, etc.

The efforts were rewarded with two absolutely clean and quiet runs, Q11 and Q12. From altogether 1620 scans 1580 passed all control criteria in the analysis; among the few rejected runs prevailed incomplete ones due to some peripheral technical problem or intervention. The background rate was stable and further reduced by 20% to 12 mHz without the necessity of pulsing off stored particles. In Q11 we applied again a random sequence like in Q10, but returned to monotonous scanning in Q12. In the last week of Q12 we ran in a slow scanning mode at 900 s per point instead of the usual 20 s interval. This way we searched for possible correlations of rates to scanning steps on an extended time scale but could not identify any.

5 Analysis of data

The way we analyze our data has been described before already [25, 27, 29] and will shortly be resumed. In the meantime, we have developed certain refinements, which we also like to apply to the already published data resulting in slight changes of the results.

5.1 Raw data selection

The raw data of a run consist of a large number of single event protocols (see above), grouped into single measurements of 20 s at particular voltage settings. With the help of the CERN routine PAW the raw data could be visualized in plots performing cuts of data and correlations of parameters. Outbursts of the count rate, e.g. caused by some sparking, were identified and rejected manually this way. In fact the total scan was rejected in case of these rare events since they were followed by a longer "afterglow" of background events. In the latest runs they did not occur at all. Also other obvious malfunctions were identified and rejected this way. This first visual data screening was followed by an automatic one which identified for each single measurement significant deviations of the voltage readings from their nominal value or their average. If they exceeded 0.1 V, the measurement was rejected. This made sure that even at the highest signal rate deep in the spectrum the corresponding signal deviation is less than 0.3σ. Moreover the program rejected single measurements when they contained more than 10 pile up events. For the remaining data it performed an automatic dead time correction reaching a level of 1% for the highest count rates. Altogether, the percentage of rejected data ranged from 2% to 6% for individual runs.

5.2 The fit function and the response function

The data from runs Q2 to Q12 were fitted each by a fit function $F(U)$, which is a convolution of the primary spectrum (2) with the response function $T'(E, U)$ of the apparatus plus a constant background b:

$$F(U) = \int (R(E)T'(E,U)\mathrm{d}E) + b = R \otimes T' + b. \quad (19)$$

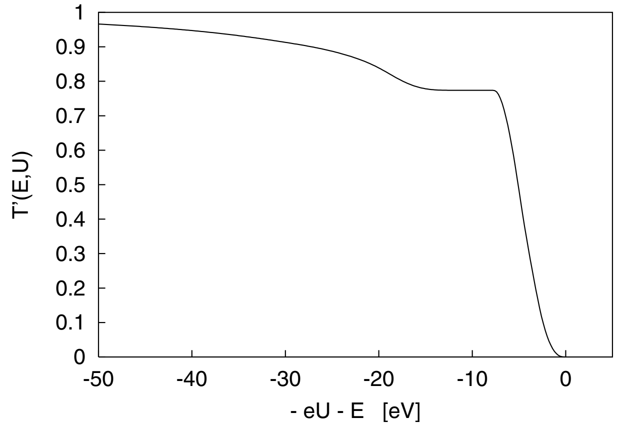

Fig. 11. Convoluted and normalized response function of the apparatus to electrons emitted at energy E and analyzed at the filter voltage U. The filter width ΔU is set to 4.8 V, the maximum starting angle to $\Theta_{\max} = 45°$ and the convolution is calculated for a source thickness of 490 Å

$T'(E,U)$ is again a fivefold convolution of the transmission function (13), the energy loss function in the film f_{loss}, the charge up potential in the film f_{charge}, the backscattering function from the substrate f_{back}, and the energy dependence of the detector efficiency f_{det}:

$$T'(E,U) = T \otimes f_{\text{loss}} \otimes f_{\text{charge}} \otimes f_{\text{back}} \otimes f_{\text{det}}. \quad (20)$$

It is plotted in Fig. 11 for an electron starting somewhere in the source with energy E and analyzed at a filter setting $U = U_a - U_s$. Its structure is dominated by $T \otimes f_{\text{loss}}$. The filter opens for the elastic component when the retarding potential $-eU$ balances the particle energy, reaching a first plateau 8 eV below. At that point the elastic component is fully transmitted. The slope of T' is stretched with respect to that of T by f_{charge} which spreads over 2.8 eV for a 140 monolayer source. The second, smaller and softer uprise results from integrating up the inelastic spectrum f_{loss}. At a setting of $-e\cdot(U+E) = -50$ eV electrons are transmitted to the detector with a chance of 98% already. f_{loss} has been determined in parallel for gaseous hydrogen as well as for shock condensed films (actually D_2) with the β electron spectrometers at Troitsk and Mainz, respectively [48]. For the condensed case, the differential cross section $d\sigma/dE$ was approximated by two model functions, a Gaussian peak at an energy loss of 14.1 eV followed by a third order hyperbola (Fig. 12). The total inelastic cross section was found in this case to be $\sigma_{\text{tot}} = (2.98 \pm 0.16) \cdot 10^{-18}\,\text{cm}^2$ with a mean energy loss of (34.4 ± 3.0) eV. As compared to the gaseous phase, it is found that the excitation peak is shifted upwards by 1.5 eV and the total cross section lowered by 13%. The shift is also confirmed by quantum chemical calculations [48]. If we define an inelastic scattering coefficient K of the film by

$$K = \sigma_{\text{tot}} \cdot \rho_N \cdot \frac{l}{\cos\Theta}, \quad (21)$$

with $l/\cos\Theta$ being the actual path length of a β particle through the film, then the probability of scattering n times

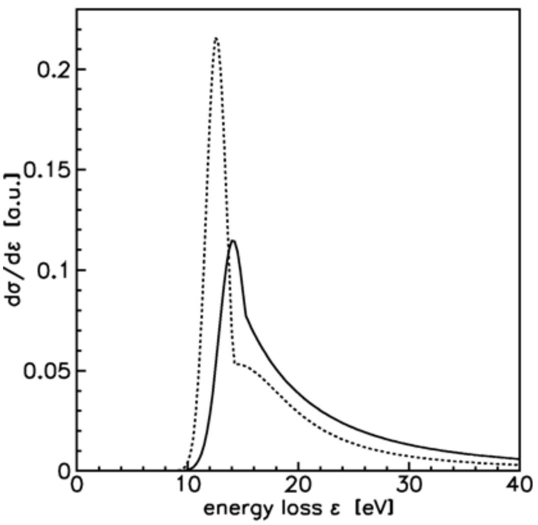

Fig. 12. Differential inelastic cross sections for 18.5 keV electrons scattered from gaseous hydrogen (dashed line) and quench condensed D_2 (solid line) [48]

is given by a Poisson distribution:

$$P_{ne} = e^{-K} K^n / n!. \quad (22)$$

At the given film thickness it is sufficient to take multiple scattering up to third order into account. The response function is obtained for each tritium film layer at a certain electrical potential – defined by f_{charge} – by an appropriate convolution of Poisson distributions (22) over energy loss and path length [48]. Running at different $\Theta_{\max}$ changes the response function, thus requiring a separate evaluation of runs.

Backscattering from the graphite substrate is quite small. Simulations have shown that its spectrum may be approximated within the interesting interval of 200 eV below the starting energy E by a constant pedestal of relative amplitude

$$\alpha_{\text{back}} = 3.1 \cdot 10^{-5}/\text{eV} \quad (23)$$

with respect to a δ-function at $E' = E$. The latter represents the transmission probability for forward emission [45]. The number given above applies to $\Theta_{\max} = 60°$. It decreases for a narrower transmission cone of $\Theta_{\max} = 50°$ to $2.3 \cdot 10^{-5}$/eV. The simulations have been checked by test experiments with K conversion electrons from ^{83m}Kr decay [45].

Since the back scattering effect is small it is sufficient to replace the exact convolution procedure by a simple correction factor,

$$f_{\text{back,corr}} = 1 + \alpha_{\text{back}}(E + eU). \quad (24)$$

The second term stands for the integral of the backscattered spectrum over the width $(E + eU)$ of the transmission window of the spectrometer. Also the folding with the energy dependent detector efficiency in (20) can be replaced by applying a simple correction factor,

$$f_{\text{det,corr}} = 1 + \alpha_d(E + eU), \quad (25)$$

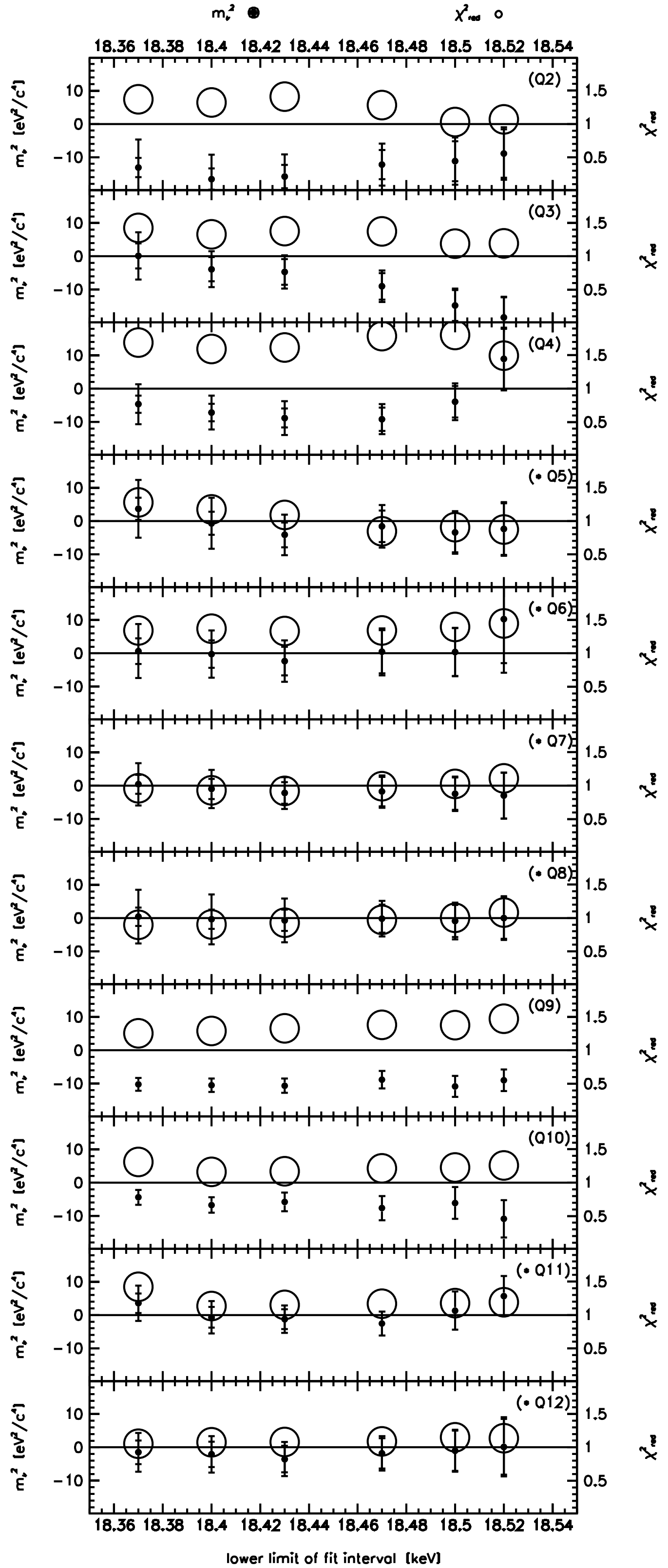

Fig. 13. Fit results of $m^2(\nu_e)$ (data points, left scale) and reduced χ^2 (circles, right scale) for runs Q2 to Q12 in dependence of the lower limit of the fit interval. The upper limit was always 18.6 keV. The inner error bars correspond to the statistical, the outer to the total uncertainty (except for Q9, Q10). The measurements used in the final analysis are marked by a star

with the coefficient mentioned before:

$$\alpha_d = (4 \pm 2) \cdot 10^{-5}/\text{eV}. \tag{26}$$

The fit is then performed with $m^2(\nu_e)$, E_0, b and a signal amplitude as free parameters.

5.3 Fits of individual runs

For all runs Q2 to Q12 fits were performed on data intervals of different spectral extension. Figure 13 shows the resulting $m^2(\nu_e)$ as a function of the lower cut off of the accepted data interval. In some cases we observe small but still significant negative $m^2(\nu_e)$ values. For runs Q4 and Q7 the corresponding fit values for E_0 are shown separately in Fig. 14. Their variation relative to that of $m^2(\nu_e)$ reflects grosso modo the correlation (10).

Figure 13 shows in addition the reduced χ^2 values for all fit intervals. In cases of negative or unstable $m^2(\nu_e)$ values they usually exceed 1, whereas they lie in the optimal range for data sets with straight $m^2(\nu_e) \approx 0$ fit results. This is seen more clearly in Fig. 15 by the comparison of the residua of the straight data set Q7 and the somewhat distorted one Q4.

5.4 Run selection for the final evaluation

The high statistics of individual runs in phase II reveals small systematic differences between their results, which have been discussed in the preceding section. Since they fall into two clear-cut classes, clean ones and those with residual problems, we may select only the former ones for the final evaluation in order to minimize systematic deviations and uncertainties and to arrive at our optimum overall result. This procedure might be considered questionable if the selection were based on a negative $m^2(\nu_e)$ result alone; because it might then introduce a bias. But we

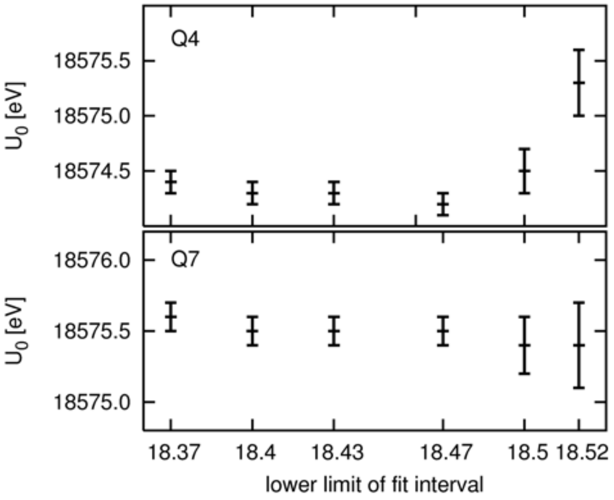

Fig. 14. Retarding voltages at which the fit finds endpoint values for runs Q4 and Q7 in dependence of the fit interval

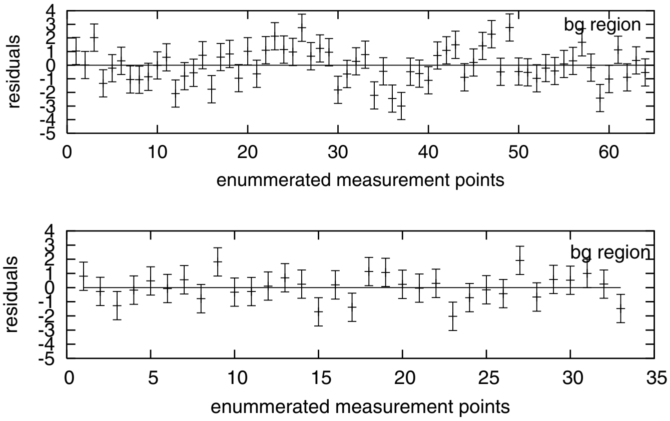

Fig. 15. Residua of fits for runs Q4 (upper part) and Q7 (lower part). The measurement points are enumerated to avoid misleading of the eyes due to unequal distances of the points. From left to right they correspond from 200 eV below to 100 eV above the endpoint E_0

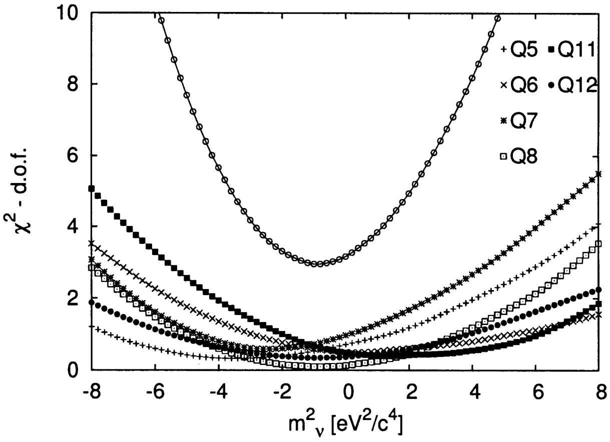

Fig. 16. Determination of $m^2(\nu_e)$ from the final data set. Shown are the χ^2 plots for the parameter $m^2(\nu_e)$ for the single data sets (different symbols) and the sum (open circles), which corresponds to the fit of the total data set. The fit intervals are restricted to a lower limit of 70 eV below E_0

have clearly shown that negative and fluctuating $m^2(\nu_e)$ values (the latter as a function of the data interval) occur at unstable running conditions, in particular with respect to background. Hence we can well justify our choice. In this sense we retain runs Q5 to Q8, Q11 and Q12 for the final analysis. It should be noted that only starting with run Q5 the very important method of applying high frequency pulses to one electrode at the detector side of the spectromter has been used in order to clean the spectrometer from possibly stored particles and to stabilize the background rate.

In detail Q2 had to be rejected because we had prepared an obviously too thick source from which we learned about the unexpected charge up effect. Here it spread over 6 eV, which is probably too much to be corrected for safely. The other four rejected runs suffered from small residual spectral anomalies of the data discussed above. Only in run Q4 we observed an anomaly whose signature was compatible with a Troitsk anomaly, i.e. a step rise in the integral spectrum. In this case one might follow the Troitsk procedure of analysis. It consists of fitting two additional parameters for position and size of the step to the data. For distinct steps lying not too close to the endpoint the additional parameters decorrelate sufficiently from the mass parameter such that the fit yields reasonably stable $m^2(\nu_e)$ values close to zero [28]. This is the case for Q4 [27] (and actually only for Q4). However, we have decided to refrain from this ad hoc procedure, since the step effect is neither stable nor properly understood (see also Sect. 6.2). This way we facilitate at least the discussion of systematic uncertainties below.

5.5 Joint analysis of selected runs

The data from the selected runs Q5 to Q8, Q11 and Q12 cannot be simply summed up for a single fit, since they have been collected at somewhat different conditions with respect to source strength, accepted solid angle, choice of measuring points etc. We also have to face slight changes of the fitted endpoint value beyond the statistical limit of order 100 meV, since we cannot guarantee the stability of our HV equipment to that level over years. Actually $m^2(\nu_e)$ is the only parameter expected to approach one and the same value in any correct data set. Therefore, we have performed a joint fit of the full data set with respect to only this parameter by the following procedure. We have first fitted each of the selected runs separately with respect to amplitude, background, and endpoint, and have calculated its χ^2 as a function of the common parameter $m^2(\nu_e)$. The six χ^2 curves were then added up to form a global χ^2 curve (Fig. 16) from which the final $m^2(\nu_e)$ fit result and its statistical error are determined. This procedure is equivalent to a common fit of all six data sets with $3 \cdot 6 + 1 = 19$ free parameters; but it converges much faster, since it makes proper use of the fact that each subset depends only on three individual and one common parameter.

5.6 Uncertainties of input parameters

For most of the input parameters entering our final fit, we adapt the same values and systematic uncertainties as chosen before in [27,29]. For the prompt neighbour excitation in solid T_2, however, we present in addition a new, critical treatment below. Some uncertainties have been quoted in Sect. 5.2 already. The others are discussed in the following.

Final states of the daughter molecule

We use the most recent calculation by Saenz et al. [38] which have been calculated for gaseous T_2 with fully satisfactory precision. In solid T_2 the excitation energy of higher excited final states shifts up slightly with respect to the ground state of $(T^3He)^+$. The effect has been estimated by Saenz [73] and is considered here with a correction of 0.8 eV for the second electronically excited state group and with 1.4 eV for the third one. This correction is also considered fully as uncertainty.

Energy loss in the T_2 film

Spectrum and cross section of energy loss have been discussed already in Sect. 5.2. The relative uncertainty of the latter is 5.4% which is added in quadrature to the one of the column density of individual runs according to Table 1.

Moreover, we consider a continuously growing coverage of the source by 0.3 monolayers of H_2 per day. This number has been obtained in two independent ways [43].
(i) Ellipsometric determination of the source thickness at the beginning and end of each run has revealed a growth of the total thickness of 0.14 monolayers per day in the average. Subtracting a T_2 loss of 0.17 monolayers/day as calculated from the apparent lifetime of the source of 400 days, yields a growing coverage by 0.31 monolayers/day.
(ii) Evaluation of data subsets from fresh and older sources shows a significant trend towards negative $m^2(\nu_e)$ values for the older ones. A coverage growth of 0.29 monolayers/day removes this dependence. The uncertainty of both results is clearly larger than their difference. Therefore the correction by 0.3 monolayers/day is also considered fully as uncertainty.

Neighbour excitation

The prompt excitation of neighbours next to a decaying T_2 molecule has been estimated by Kolos in sudden approximation [39]. The effect is due to the local relaxation of the lattice following the sudden appearance of an ion. A rigorous calculation of final states of the surrounding electron cloud is still missing. Therefore, it is difficult to assign a proper uncertainty to Kolos' estimated excitation probability of $P_{ne} = 0.059$ with a mean energy of 14.6 eV. The latter number applies to the excitation spectrum of free hydrogen molecules. It seems reasonable to increase this number by the same 1.5 eV by which the energy loss spectrum of electrons is shifted upwards (compare Sect. 5.2). In the same sense, the corresponding reduction of the total inelastic cross section by 13% [48] has been applied also to P_{ne} in our former standard analysis. Another reduction of P_{ne} by 11% has been accounted for the observed porosity of our shock condensed films (see Sect. 3.1), yielding finally $P_{ne} = 0.046$. This number has also been used in [27], although it has been composed from slightly different factors. Since the shifts in excitation energy and probability, applied to Kolos' calculated values, are based but on qualitative, plausible arguments, they had entered also fully the systematic uncertainty.

The large, consistent data basis available now gives us a handle to try a self-consistent determination of P_{ne} by treating it as an additional free parameter in a joint analysis of a large interval comprising data down to 170 eV below E_0 where the inelastic components really matter. Figure 17 shows the resulting χ^2 contour plot in the $(P_{ne}, m^2(\nu_e))$ plane. Its minimum lies at $P_{ne} = 0.050 \pm 0.016$ and $m^2(\nu_e) = (0 \pm 3.3)\,\mathrm{eV}^2/c^4$, a very satisfactory result, indeed. It confirms our former estimated value of $P_{ne} = 0.046$ within errors and lifts the former tendency towards slightly negative $m^2(\nu_e)$ values for the entire data set (see below).

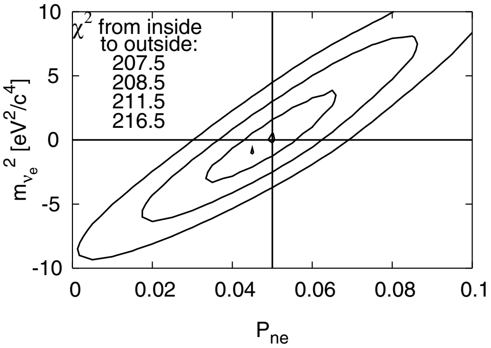

Fig. 17. Shown are contour plots of $\chi^2(P_{ne}, m^2(\nu_e))$ at 1σ, 2σ and 3σ around its minimum value at $(0.05, 0)$

Still this fit value of P_{ne} is subject to a quite sizable systematic uncertainty of ±0.022. It stems from its strong correlation to the energy loss in the film due to their similar effect on the spectrum. The uncertainty for energy losses are a combination of the uncertainty of the determination of the film thickness and the measurement of the total cross section σ_{tot}. The averaged uncertainty in measuring the film thickness for all accepted runs is 3% and the uncertainty of σ_{tot} is 5.4%. In order to determine the correlation of P_{ne} and $\sigma_{\mathrm{tot}}\rho d$ [5] we have calculated the χ^2 contour plot of Fig. 17 for different values of $\sigma_{\mathrm{tot}}\rho d$ and located its minimum in the $(P_{ne}, m_{\nu_e}^2)$-space each time. The corresponding $(P_{ne}, \sigma_{\mathrm{tot}}\rho d)$- pairs are plotted in Fig. 18. We see an almost straight anticorrelation of the two energy loss contributions. The correlation transfers the uncertainty of $\sigma_{\mathrm{tot}}\rho d$ directly into one of P_{ne} as indicated by the bars in Fig. 18. $m^2(\nu_e)$ and χ^2 are rather insensitive to this exchange of $\sigma_{\mathrm{tot}}\rho d$ and P_{ne}. In particular, we cannot fix $\sigma_{\mathrm{tot}}\rho d$ separately by the fit alone better than by external input.

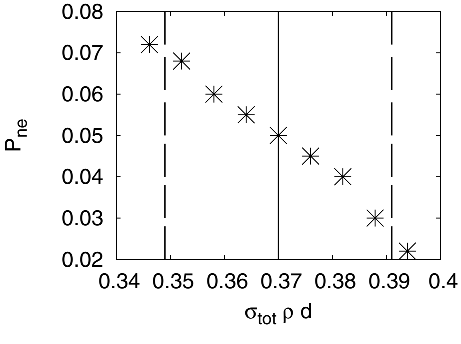

Fig. 18. Correlation between neighbour excitation probability P_{ne} and $\sigma_{\mathrm{tot}}\rho d$. Each point corresponds to the center of a contour plot like in Fig. 17, calculated for particular values of $\sigma_{\mathrm{tot}}\rho d$ within its 1σ uncertainty interval (0.370 ± 0.023), indicated by the vertical lines

---

[5] $\sigma_{\mathrm{tot}}\rho d$ is a measure for the scattering probability in the tritium film.

Self-charging of T_2 film

It has been found that the film charges up within 30 min to a constant critical field strength of 62.6 MV/m [71]. It results in a linearly increasing shift of the starting potential of β particles throughout the film, reaching about 2.5 V at the outer surface. We have assigned a conservative systematic uncertainty of ±20% to that slope.

Backscattering and detector efficiency

Both effects are small and can be accounted for by the linear correction factors (23), (24) and (25), (26) given above. They may just be contracted into a single correction factor

$$f_{\text{backcorr}} \cdot f_{\text{dcorr}} \approx 1 + (\alpha_{\text{back}} + \alpha_d)(E + eU). \qquad (27)$$

In (26) we have already assigned to α_d a conservative uncertainty of $\pm 2 \cdot 10^{-5}$/eV, which is large enough to cover a residual uncertainty of α_{back} as well.

5.7 Systematic uncertainty of $m^2(\nu_e)$

In the standard analysis the systematic uncertainty of $m^2(\nu_e)$ is calculated from those of the external input parameters as follows: Each input parameter is shifted from its best value by its uncertainty and the fit to a particular data set is repeated. The resulting shift of the χ^2 minimum with respect to $m^2(\nu_e)$ is then taken as the corresponding systematic uncertainty of $m^2(\nu_e)$.

The systematic uncertainty of the joint data set is evaluated in the standard analysis by the same procedure. Figure 19 shows for the joint data set the individual contributions as well as the quadratically summed up uncertainties calculated for different lengths of the data interval. Obviously the statistical uncertainty decreases with the length of the interval whereas the systematic increases. The total, combined uncertainty attains a flat minimum of $\Delta m^2_{\text{tot}} = 3.04\,\text{eV}^2/c^4$ for a lower cut off at $E_{\text{low}} = 18500$ eV which is regarded the optimum interval, therefore.

Summarizing, the standard analysis with the external input parameter of neighbour excitation probability $P_{ne} = (0.046 \pm 0.013)$ yields for the optimal data interval the result

$$m^2(\nu_e)_{\text{standard}} = (-1.2 \pm 2.2_{\text{stat}} \pm 2.1_{\text{syst}})\,\text{eV}^2/c^4;$$
$$\chi^2/\text{d.o.f.} = 208/195. \qquad (28)$$

Here the uncertainties of the externally chosen, independent parameters P_{ne} and $\sigma_{\text{tot}}\rho d$ contribute to that of $m^2(\nu_e)$ by an amount of

$$\delta m^2(\nu_e)_{\text{syst,ext}}(P_{ne}, \sigma_{\text{tot}}\rho d) = 1.59\,\text{eV}^2/c^4. \qquad (29)$$

Using the self-consistently fitted P_{ne} value instead, we have to take into account that its systematic uncertainty of ±0.022 is anticorrelated to the corresponding uncertainty of ∓0.023 of $\sigma_{\text{tot}}\rho d$ according to Fig. 18. Their combined action on $m^2(\nu_e)$ has to be calculated, therefore. Moreover, we have to consider the statistical uncertainty $\delta P_{\text{ne,stat}} = \pm 0.016$, which results from the fit in Fig. 17. Added in quadrature to the systematic contribution we obtain from the self-consistent analysis for the optimum interval $E > 18500$ eV a combined systematic uncertainty of

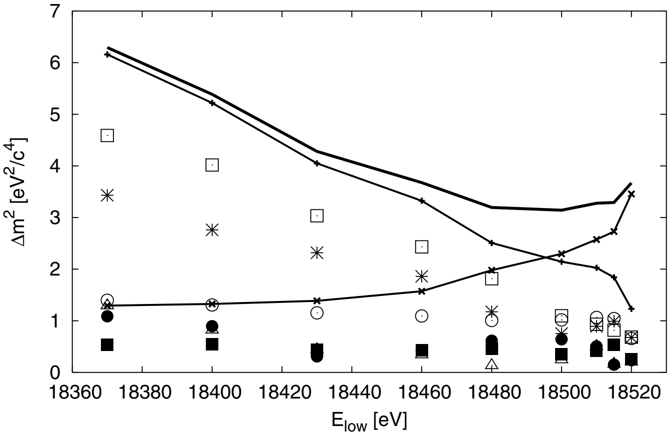

Fig. 19. Individual and quadratically summed up uncertainties of $m^2(\nu_e)$ for the joint data set, calculated for different lengths of the data interval. The open squares and stars give the contribution of energy losses in the tritium film, the open circles the neighbour excitation, the filled squares the self-charging effect, the filled circles the final states and the open triangles the detector efficiency. The line with simple crosses shows the sum of systematic uncertainties in dependence from the fit interval and the line with stars gives the corresponding statistical uncertainty (growing). The upper most line gives the quadratically summed up values and has its minimum for 18500 eV

$$\delta m^2(\nu_e)_{\text{syst,selfcons.}}(P_{ne}, \sigma_{\text{tot}}\rho d) = 1.58\,\text{eV}^2/c^4. \qquad (30)$$

The marginal reduction compared to (29) would not really be worth the effort. Rather we emphasize that it determines for the first time the probability of neighbour excitation from the data themselves and confirms, moreover, the qualitative estimation of correction factors applied earlier to Kolos' original calculation of P_{ne} [39].

In addition the slight shift of the central value of P_{ne} from 0.046 in the standard analysis to 0.05 in the self-consistent one causes a corresponding shift of the $m^2(\nu_e)$ fit value of the final result still closer to zero:

$$m^2(\nu_e) = (-0.6 \pm 2.2_{\text{stat}} \pm 2.1_{\text{syst}})\,\text{eV}^2/c^4$$
$$\chi^2/\text{d.o.f.} = 208/194. \qquad (31)$$

6 Discussion of results

6.1 Experimental β spectrum

We start the discussion by taking a look at the measured spectra in the vicinity of the endpoint (Fig. 20). The bulk of phase II data has been obtained in runs Q5 to Q8 under almost identical conditions and may hence be composed here into a single spectrum (full squares). The open squares

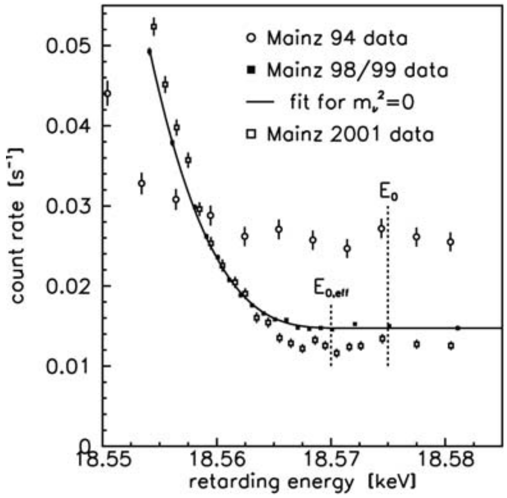

Fig. 20. Averaged count rate of the 98/99 data (filled squares) with fit for $m^2(\nu_e) = 0$ (line) and the 2001 data (open squares) in comparison with previous Mainz data from phase I (open circles) plotted as a function of the retarding potential near the endpoint E_0

represent runs Q11 and Q12. The rate is slightly higher and the background still lower than in the Q5 to Q8 runs. For comparison we also show the last spectrum from phase I taken in 1994 (open circles) [26, 59]. The full curve is a fit to the Q5 to Q8 data with $m^2(\nu_e)$ fixed to zero, looking perfect. Already 5 eV below the effective endpoint the spectrum rises distinctly from the background, excluding prima vista any larger neutrino mass. (The shift of the effective endpoint from the true one is obtained from an average over the ro- vibrational excitation of the daughter molecule, over the transmission function, and over the source charging.) Moreover, these summed up data exclude safely any steady spectral anomaly close to the endpoint on the level of 1 mHz; this corresponds to about 10^{-12} of the total decay rate of the source.

6.2 Troitsk anomaly

The absence of any anomaly in the summed up spectrum does not exclude necessarily a steplike Troitsk anomaly which would fluctuate in position and amplitude. It might be washed out in the summed up data. Indeed it has been observed to be a fluctuating effect, for some time hinting to a half year period even [28]. In December 2000, however, it appeared as a sudden outburst [74]. In this period Q10 was running at Mainz in parallel. Figure 21 shows the analysis of both runs with respect to the appearance of a step in the integral spectrum, i.e. a line in the original spectrum. To that end one fits the spectrum to the data under the assumption of an additional sharp line of free amplitude at a particular position. The upper plot shows the course of χ^2 as a function of the line position for the Troitsk data. A very significant minimum is observed at 18553 eV indicating a line, (or step, respectively) with an equally significant amplitude of 13 mHz (middle plot). The corresponding χ^2 plot for the parallel run at Mainz with similar sensitivity shows but fluctuations of statistical size (lower plot). Hence speculations that the Troitsk anomaly might be due to a fluctuating presence of dense neutrino clouds [28] are disproved. Rather it has to be attributed to instrumental effects, as pointed out already in Sect. 4.2 (see also [36, 44]).

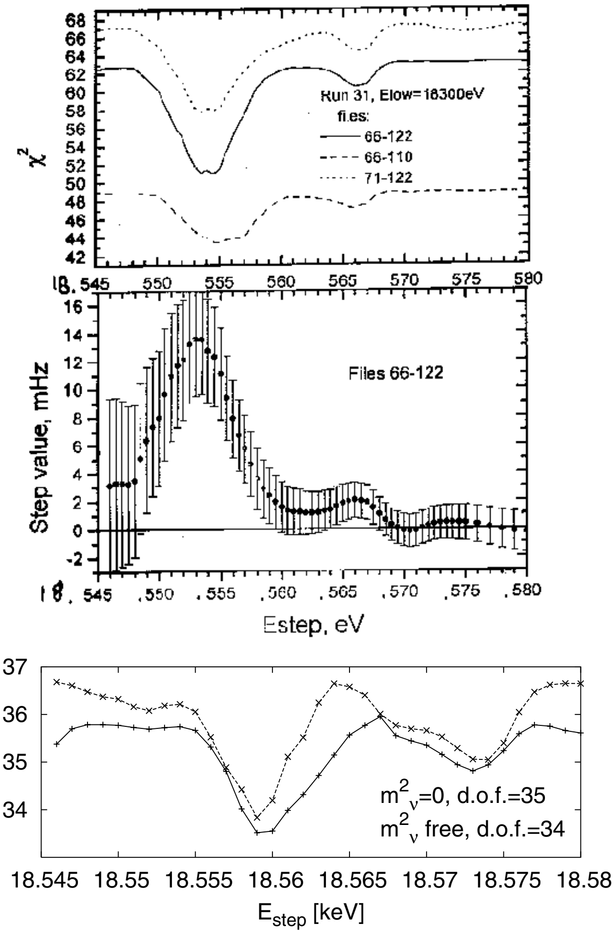

Fig. 21. Search for a steplike anomaly in parallel measurements in December 2000. The upper and the middle graph show the analysis of the Troitsk data [74] by adding position and amplitude of the step as free parameters. The upper graph shows the resulting drop of χ^2, the lower one the fitted step amplitude, both as function of the step position. A very significant signal appears around 18553 eV. In contrast the corresponding χ^2 plot for the Mainz data (lower graph) is shown, fluctuations are insignificantly by only 2 units

6.3 $m^2(\nu_e)$ result and upper limit of $m(\nu_e)$

From the two alternative choices of the neighbour excitation probability we settle on the self-consistently determined one for reasons given in Sects. 5.6 and 5.7. Hence (31) is our final experimental result on the observable $m^2(\nu_e)$. As compared to our earlier communicated result [29] it has improved in three respects.
(1) The statistical uncertainty has been diminished further by 0.3 eV$^2/c^4$.

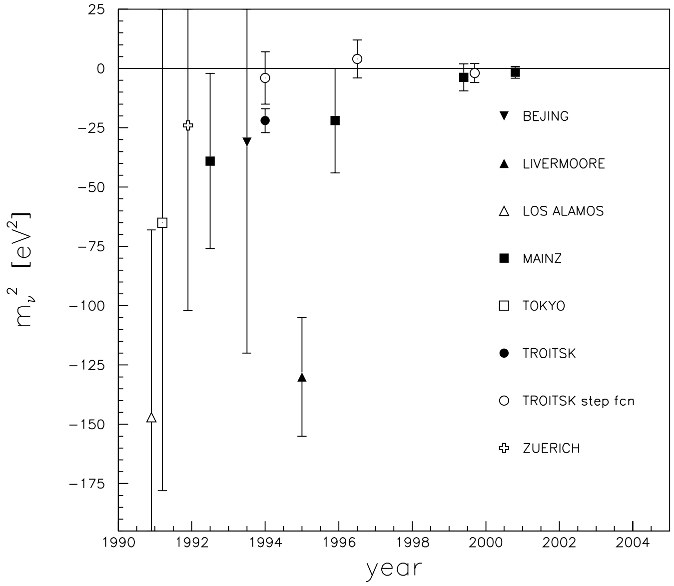

Fig. 22. Published results of squared neutrino mass values $m^2(\nu_e)$ obtained from tritium decay since 1990. The already finished experiments at Los Alamos, Zürich, Tokyo, Beijing and Livermore [76–80] used magnetic spectrometers, the experiments at Troitsk and Mainz are using MAC-E-Filters (as described before)

(2) The systematic uncertainty has been better founded with respect to the questionable neighbour excitation probability (but remained unchanged in size).
(3) The central value has moved further up from $-1.6\,\mathrm{eV}^2/c^4$ to $-0.6\,\mathrm{eV}^2/c^4$ and has lost by now any touch of being unphysical in view of the error bars.

The progress in the observable $m^2(\nu_e)$ of this final Mainz result as compared to the most sensitive earlier experiments using momentum analyzing spectrometers approaches 2 orders of magnitude (Fig. 22). The Troitsk group communicated similar numbers [75] ($m^2(\nu_e) = (-2.3 \pm 2.5_{\mathrm{stat}} \pm 2.0_{\mathrm{syst}})\,\mathrm{eV}^2/c^4$), but there is an important difference. The Troitsk group needs to correct for the observed anomaly by adding phenomenologically a sharp line with free position and size to the β spectrum without including a systematic correction for this approach. Without this correction the fit would charge this effect on $m^2(\nu_e)$ and drive it negative as discussed above already. Since phenomenology and origin of the anomaly are barely known, this procedure is not obvious and it is difficult to assign a proper systematic uncertainty to this correction. Up to now the Troitsk group has not considered in its result any systematic uncertainty of this correction.

If we move the central value of $m^2(\nu_e)$ to zero and calculate from there the upper mass limit at 95% C.L., then we obtain the so-called sensitivity limit. It lies for both evaluations (28) and (31) at

$$m_{\mathrm{sens.\ lim.}}(\nu_e) = 2.4\,\mathrm{eV}/c^2, \quad (95\%\ \mathrm{C.L.}). \qquad (32)$$

Since the actual $m^2(\nu_e)$ values are slightly negative we derive from them an upper limit by help of the unified approach [81], recommended by the particle data group. This yields in case of the result (28) from the standard analysis

$$m(\nu_e) < 2.2\,\mathrm{eV}/c^2, \quad (95\%\ \mathrm{C.L.}), \qquad (33)$$

which agrees with the latest communicated value [29]. Our preferred result (31), however, calculated with a self-consistent P_{ne} value, yields a slightly higher limit:

$$m(\nu_e) < 2.3\,\mathrm{eV}/c^2, \quad (95\%\ \mathrm{C.L.}), \qquad (34)$$

since the respective $m^2(\nu_e)$ value lies still closer to zero. The increasing reduction of the upper limit below the sensitivity limit as a function of an increasing negative $m^2(\nu_e)$ value is but a dubious gift of the unified approach, accompanied by an increase of the probability that the result suffers from unidentified systematic errors. We quote (34) instead of (32) or (33) as our final upper mass limit, because it stems from a more consistent analysis of the data on one hand and conforms to the recommended unified approach on the other. Anyway, their difference is marginal.

7 Conclusion and outlook

Phase II of the Mainz neutrino mass experiment started in 1995 with substantial improvements regarding the frozen T_2 source as well as background rejection in the β transport channel and in the electrostatic spectrometer. This enabled running at a 10 times better signal to background ratio from 1997 on. Thereafter, a number of side experiments yielded the following.
(1) A detailed study and suppression of the unexpected and disturbing dewetting of the T_2 film from the substrate [46,47].
(2) The discovery, quantification and theoretical explanation of source charging [71].
(3) A determination of the energy loss spectrum of β particles in solid T_2 [48].
(4) Phenomenological studies and suppression of background mechanisms in MAC-E Filters.

These issues formed the basis for a satisfactory control and reduction of systematic uncertainties in parallel to the statistical one.

Data taking on the search for the neutrino mass covered the years 1998 to 2001 and yielded the so far narrowest limit on the observable $m^2(\nu_e)$ of $(-0.6 \pm 3.0)\,\mathrm{eV}^2/c^4$ from which an upper limit $m(\nu_e) < 2.3\,\mathrm{eV}/c^2$ (90% C.L.) is derived.

The discovery of neutrino oscillations at squared mass differences of $\Delta m_{ij}^2 \leq 0.05\,\mathrm{eV}^2/c^4$ [1–10] allows one furthermore to apply the same upper limit to all three neutrino flavors as reference value in particle and astrophysics. Clearly there is a burning interest to improve this limit further in order to check cosmological models more sensitively by laboratory results on one hand and to decide on the alternative between degenerate and hierarchical neutrino masses on the other. In this respect a recent paper on the final data from the Heidelberg–Moscow experiment is giving a first indication; it reports on a 4σ signal of neutrinoless double β decay in ^{76}Ge [12]. Explained by an exchange of a massive Majorana neutrino, this signal would give a mass in the approximate limits $0.1 \leq m_{ee}c^2/\mathrm{eV} \leq 0.9$ (95% C.L.).

Obviously our present experiment has exhausted its potential by now, almost 20 years after it has been first conceived. First plans to build either a rigorously enlarged MAC-E-Filter [70], or a bent variant offering in addition a highly resolving differential energy analysis [82] were proposed at an Erice meeting in 1997. A following paper treated in some detail the potential of a MAC-E-Filter of 5 m diameter and reported moreover on an implementation of a time of flight mode which transforms a MAC-E-Filter from a high pass to a narrow band filter with equally sharp slopes [68]. In 2000 the KATRIN collaboration [57] formed, proposing to build a large MAC-E-filter in combination with a gaseous T_2 source at the site of the Forschungszentrum Karlsruhe. It combines the expertise from the foregoing experiments at Los Alamos [72], Mainz and Troitsk with the strength of a national laboratory including expertise in handling large amounts of tritium. The present design aims at reaching within three years of measurement a precision of $\Delta m^2(\nu_e) \approx 0.02\,\mathrm{eV}^2/c^4$ corresponding to a sensitivity limit of $0.2\,\mathrm{eV}/c^2$ for the mass itself. The experiment should be ready to go in 2008.

Acknowledgements. The authors are grateful to the Deutsche Forschungsgemeinschaft, which supported this experiment under contract no. Ot33 from its beginning until 2000 and to the Bundesministerium für Bildung und Wissenschaft which took over thereafter under contract no. 06Mz866I/5. Our thanks also go to our frequent guests from Troitsk, V. Lobashev (supported by an Alexander von Humboldt Award), as well as O. Kazachenko and N. Titov (supported by a visitor programme of the Deutsche Forschungsgemeinschaft) for their valuable contributions.

References

1. S. Fukuda and the Superkamiokande Collaboration, Phys. Rev. Lett. **81**, 1562 (1998)
2. R. Davis, Nucl. Phys. B (Proc. Suppl.) **48**, 284 (1996)
3. M.B. Smy and the Superkamiokande Collaboration, Nucl. Phys. B (Proc. Suppl.) **118**, 25 (2003)
4. B.T. Cleveland et al., Astrophys. J. **496**, 505 (1998)
5. T.A. Kirsten and the GNO Collaboration, Nucl. Phys. B (Proc. Suppl.) **118**, 33 (2003)
6. V.N. Garvin and the SAGE Collaboration, Nucl. Phys. B (Proc. Suppl.) **118**, 39 (2003)
7. A.L. Hallin and the SNO Collaboration, Nucl. Phys. B (Proc. Suppl.) **118**, 3 (2003)
8. Q.R. Ahmad et al., Phys. Rev. Lett. **89**, 011301 (2002)
9. K. Eguchi and the KamLAND Collaboration, Phys. Rev. Lett. **90**, 021802 (2003)
10. M.C. Gonzalez-Garcia, Y. Nir, Rev. Mod. Phys. **75**, 345 (2003)
11. H.V. Klapdor-Kleingrothaus, A. Dietz, H.L. Harney, I.V. Krivosheina, Mod. Phys. Lett. A **16**, 2409 (2001)
12. H.V. Klapdor-Kleingrothaus, I.V. Krivosheina, A. Dietz, O. Chkvorets, Phys. Lett. B **586**, 198 (2004)
13. D.N. Spergel et al., astro-ph/0302209 (2003), Astrophys. J. (Suppl.) **148**, 175 (2003)
14. S. Hannestad, JCAP **0305**, 004 (2003), astro-ph/0303076 (2003)
15. V. Barger, D. Marfatia, A. Regre, hep-ph/0312065 v2 (2003)
16. S.W. Allen, A.C. Fabian, S.L. Fridle, astro-ph/0306386 (2003)
17. R.G.H. Robertson, D.A. Knapp, Ann. Rev. Nucl. Sci. **38**, 185 (1988)
18. E. Holzschuh, Rep. Proc. Phys. **55**, 1035 (1992)
19. J.F. Wilkerson, R.G.H. Robertson, in Current Aspects Of Neutrino Physics, edited by D.O. Caldwell (Springer, Berlin, Heidelberg 2001), p. 39
20. Ch. Weinheimer, in Neutrino Mass, edited by G. Altarelli and K. Winter, Springer Tracts in Modern Physics **190**, (Springer-Verlag, Berlin, Heidelberg, Germany 2003), p. 25
21. A. Picard, H. Backe, H. Barth, J. Bonn, B. Degen, Th. Edling, R. Haid, A. Hermanni, P. Leiderer, Th. Loeken, A. Molz, R.B. Moore, A. Osipowicz, E.W. Otten, M. Przyrembel, M. Steininger, Ch. Weinheimer, Nucl. Instr. Meth. B **63**, 345 (1992)
22. V.M. Lobashev, P.E. Spivac, Phys. Lett. B **460**, 3305 (1985)
23. A.I. Belesev et al., Phys. Lett. B **350**, 263 (1995)
24. Christian Weinheimer, Doct. Thesis, Mainz University (1993)
25. Ch. Weinheimer, M. Przyrembel, H. Backe, H. Barth, J. Bonn, B. Degen, Th. Edling, H. Fischer, L. Fleischmann, J.U. Grooß, R. Haid, A. Hermanni, G. Kube, P. Leiderer, Th. Loeken, A. Molz, R.B. Moore, A. Osipowicz, E.W. Otten, A. Picard, M. Schrader, M. Steininger, Phys. Lett. B **300**, 210 (1993)
26. H. Backe, H. Barth, A. Beile, J. Bonn, B. Degen, L. Fleischmann, M. Gundlach, E.W. Otten, M. Przyrembel, Ch. Weinheimer in Proceedings 17. International Conference on Neutrino Physics and Astrophysics, Helsinki, Finnland, June 1996 (World Scientific, Singapore), p. 259
27. Ch. Weinheimer, B. Degen, A. Bleile, J. Bonn, L. Bornschein, O. Kazachenko, A. Kovalik, E.W. Otten, Phys. Lett. B **460**, 219 (1999)
28. V.M. Lobashev et al., Phys. Lett. B **460**, 227 (1999)
29. J. Bonn, B. Bornschein, L. Bornschein, L. Fickinger, B. Flatt, O. Kazachenko, A. Kovalik, Ch. Kraus, E.W. Otten, J.P. Schall, H. Ulrich, Ch. Weinheimer, Nucl. Phys. B (Proc. Suppl.) **91**, 273 (2001)
30. R.S. Van Dyck, Jr., D.L. Farnham, P.B. Schwinberg, Phys. Rev. Lett **70**, 2888 (1993)
31. J.J. Simpson, Phys. Rev. D **23**, 64 (1981)
32. W.W. Repco, C.E. Wu, Phys. Rev. C **28**, 2433 (1983)
33. S. Gardner, V. Bernard, U.-G. Meißner, Phys. Lett. B **598**, 188 (2004)
34. G.J. Stephenson, T. Goldman, Phys. Lett. B **440**, 89 (1998)
35. Particle Data Group, Phys. Rev. D **66**, 321 (2002)
36. Christine Kraus, Diploma Thesis, Mainz University (2000)
37. O. Fackler, B. Jeziorski, W. Kolos, H.J. Monkhorst, K. Szalewicz, Phys. Rev. Lett. **55**, 1388 (1985)
38. A. Saenz, S. Jonsell, P. Froehlich, Phys. Rev. Lett. **84**, 242 (2000)
39. W. Kolos et al., Phys. Rev. A **37**, 2297 (1988)
40. E.W. Otten, Prog. Part. Nucl. Phys. **32**, 153 (1994)
41. A. Picard, H. Backe, J. Bonn, B. Degen, R. Haid, A. Hermanni, P. Leiderer, A. Osipowicz, E.W. Otten, M. Przyrembel, M. Schrader, M. Steininger, Ch. Weinheimer, Z. Phys. A **342**, 71 (1992)
42. Beate Bornschein, Doct. Thesis, Mainz University (2000)
43. Lutz Bornschein, Doct. Thesis, Mainz University (2002)

44. Christine Kraus, Doct. Thesis, Mainz University (2004)
45. Lars Fleischmann, Doct. Thesis, Mainz University (1998)
46. L. Fleischmann, J. Bonn, B. Degen, M. Przyrembel, E.W. Otten, Ch. Weinheimer, P. Leiderer, J. Low Temp. Phys. **119**, 615 (2000)
47. L. Fleischmann, J. Bonn, B. Bornschein, P. Leiderer, M. Przyrembel, Ch. Weinheimer, A. Saenz, Eur. Phys. J. B **16**, 521 (2000)
48. V.N. Aseev, A.I. Belesev, A.I. Berlev, E.V. Geraskin, O.V. Kazachenko, Yu.E. Kuznetsov, V.M. Lobashev, R.P. Ostroumov, N.A. Titov, S.V. Zadorozhny, Yu.I. Zakharov, J. Bonn, B. Bornschein, L. Bornschein, E.W. Otten, M. Przyrembel, Ch. Weinheimer, A. Saenz, Eur. Phys. J. D **10**, 39 (2000)
49. R. Conradt, U. Albrecht, S. Herminghaus, P. Leiderer, Physica B **194**–**196**, 679 (1994)
50. Oliver Kettig, Dipl. Thesis, Mainz University (1994)
51. R.M.A. Azzam, N.M. Bashara, Ellipsometry and polarized light (North Holland Publ. Comp, Amsterdam, Netherlands 1988)
52. W. Kolos, L. Wolniewicz, J. Chem. Phys. **46**, 1426 (1967)
53. I. Silvera, Rev. Mod. Phys. **52**, 393 (1980)
54. Hermann Fischer, Dipl. Thesis, Mainz University (1980)
55. Herbert Barth, Dipl. Thesis, Mainz University (1991)
56. Daphne Goldmann, Dipl. Thesis, Mainz University (1995)
57. A. Osipowicz et al., hep-ex/0109033
58. V.M. Lobashev, Troitsk, private communication
59. Herbert Barth, Doct. Thesis, Mainz University (1997)
60. Ch. Weinheimer, M. Schrader, J. Bonn, Th. Loeken, H. Backe, Nucl. Instrum. Methods A **311**, 273 (1993)
61. Holger Ulrich, Dipl. Thesis, Mainz University (2000)
62. Jean-Pierre Schall, Dipl. Thesis, Mainz University (2001)
63. Beatrix Müller, Dipl. Thesis, Mainz University (2002)
64. Frank Schwamm, Doct. Thesis, Karlsruhe University (2004)
65. Thomas Thümmler, Dipl. Thesis, Mainz University (2002)
66. Salvadore Sanchez, Dipl. Thesis, Mainz University (2003)
67. Björn Flatt et al., to be published
68. J. Bonn, L. Bornschein, B. Degen, E.W. Otten, Ch. Weinheimer, Nucl. Instr. Meth. A **421**, 256 (1999)
69. J. Ciborowski, J. Rembielinski, Eur. Phys. C **8**, 157 (1999)
70. H. Barth, L. Bornschein, B. Degen, L. Fleischmann, M. Przyrembel, H. Backe, A. Bleile, J. Bonn, D. Goldmann, M. Gundlach, O. Kettig, E.W. Otten, G. Tietze, Ch. Weinheimer, P. Leiderer, O. Kazachenko, A. Kovalik, Prog. Part. Nucl. Phys. **40**, 353 (1998)
71. B. Bornschein, J. Bonn, L. Bornschein, E.W. Otten, Ch. Weinheimer, J. Low Temp. Phys. **131**, 69 (2003)
72. J.F. Wilkerson et al., Phys. Rev. Lett. **58**, 2023 (1987)
73. A. Saenz, Humboldt University, Berlin, private communication
74. V.M. Lobashev, talk and Proceedings International Conference on Non-Accelerator New Physics, Dubna, 2001
75. V.M. Lobashev, Proceedings 17. International Conference on Nuclear Physics in Astrophysics, Debrecen/Hungary, 2002, Nucl. Phys. A **719**, 153c–160c (2003)
76. R.G.H. Robertson et al., Phys. Rev. Lett. **87**, 957 (1991)
77. E. Holzschuh et al., Phys. Lett. B **287**, 381 (1992)
78. H. Kawakami et al., Phys. Lett. B **256**, 105 (1991)
79. H.C. Sun et al., CJNP **15**, 261 (1993)
80. W. Stoeffl, D.J. Decman, Phys. Rev. Lett. **75**, 3237 (1995)
81. G.J. Feldmann, R.D. Cousins, Phys. Rev. D **57**, 3873 (1998)
82. V.M. Lobashev, Prog. Port, Nucl. Phys. **40**, 337 (1998)